Published in final edited form as:
Nature. 2021 April 01; 592(7852): 144–149. doi:10.1038/s41586-021-03374-w.

DNA-driven condensation assembles the meiotic DNA break machinery

Corentin Claeys Bouuaert[1,2,*], **Stephen Pu**[1], **Juncheng Wang**[3], **Cédric Oger**[2], **Dima Daccache**[2], **Wei Xie**[3], **Dinshaw J. Patel**[3], **Scott Keeney**[1,*]

[1]Molecular Biology Program, Memorial Sloan Kettering Cancer Center and Howard Hughes Medical Institute, New York, US

[2]Louvain Institute of Biomolecular Science and Technology, Université catholique de Louvain, Louvain-La-Neuve, Belgium

[3]Structural Biology Program, Memorial Sloan Kettering Cancer Center, New York, US

Abstract

Accurate segregation of chromosomes during meiosis—critical for genome stability across sexual cycles—relies on homologous recombination initiated by DNA double-strand breaks (DSBs) made by the Spo11 protein[1,2]. DSB formation is regulated and tied to the elaboration of large-scale chromosome structures[3–5], but the protein assemblies that execute and control DNA breakage are poorly understood. We address this through molecular characterization of *Saccharomyces cerevisiae* RMM proteins (Rec114, Mei4 and Mer2)—essential, conserved components of the DSB machinery[2]. Each subcomplex of Rec114–Mei4 (a 2:1 heterotrimer) or Mer2 (a coiled-coil-containing homotetramer) is monodisperse in solution, but they independently condense with DNA into reversible nucleoprotein clusters that share properties with phase-separated systems. Multivalent interactions drive condensation. Mutations that weaken protein–DNA interactions strongly disrupt both condensate formation and DSBs *in vivo*, strongly correlating these processes. *In vitro*, condensates fuse into mixed RMM clusters that further recruit Spo11 complexes. Our data show how the DSB machinery self-assembles on chromosome axes to create centers of DSB activity. We propose that multilayered control of Spo11 arises from the recruitment of regulatory components and modulation of biophysical properties of the condensates.

*Correspondence and requests for materials should be addressed to CCB or SK. corentin.claeys@uclouvain.be (C.C.B.), s-keeney@ski.mskcc.org (S.K.).

Author contributions: C.C.B. and S.K. designed the study and supervised the research; C.C.B. carried out all experiments except as noted; S.P. performed yeast-two-hybrid experiments (Fig. 4g, Extended Data Fig 1k, 8e) and assisted C.C.B with the generation of expression constructs, virus preparations and protein purifications; J.W. performed SEC-MALS analyses of mutant protein constructs (Fig. 1j, Extended Data Fig. 1h, j) and W.X. performed FRAP experiments (Extended Data Fig. 5c), under supervision of D.J.P.; C.O. performed MBP pulldown (Extended Data Fig. 7d) and trypsin proteolysis experiments (Extended Data Fig. 6h) and D.D. performed the condensate mixing experiments in Extended Data Figs. 6e and 8f, under supervision of C.C.B.; C.C.B. and S.K. wrote the paper with input from the other authors; C.C.B., D.J.P. and S.K. secured funding.

Authors declare no competing interests.

Europe PMC Funders Author Manuscripts

In *S. cerevisiae*, DSB formation involves the coordinated action of ten proteins in three subgroups[2]. Spo11, Rec102, Rec104 and Ski8 form the DSB enzyme ("core complex") related to archaeal topoisomerases[6–10]; the MRX (Mre11, Rad50 and Xrs2) complex is also important for the processing of DSBs[2]; and the third subgroup comprises the RMM proteins, which have been grouped together based on yeast-two-hybrid (Y2H) interactions, coimmunoprecipitation, and foci colocalization and interdependencies[11–14].

RMM proteins lie at the crossroads between DSB formation and chromosome organization: they associate with chromatin early in meiotic prophase and form overlapping, interdependent foci along chromosome axes[11,12,15,16]. They interact with other components of the DSB machinery and the hotspot-targeting protein Spp1, thereby connecting chromosome axes with sites of DNA cleavage[12,17–19]. RMM proteins are conserved, albeit with high sequence divergence[20–24], but their functions and biochemical properties remain enigmatic (Supplementary Discussion 1).

Heterotrimeric Rec114–Mei4 complexes

Because of long-known functional relationships between Rec114, Mei4 and Mer2[11,12,17], confirmed in other species[14,21,23,25], we sought to purify a tripartite complex. However, while Mer2 alone and a Rec114–Mei4 complex were readily purified, we could not obtain a stable RMM complex (Extended Data Fig. 1a, b).

Much of Rec114 is predicted as disordered (Fig. 1a, top). The N-terminal region contains six signature sequence motifs (SSMs), with a seventh located near the C terminus[12,23,26]. The N-terminal SSMs of mouse REC114 form a pleckstrin homology (PH)-like fold[25,27]. Mei4 is mostly ordered (Fig. 1a, bottom), with six SSMs[26].

Europe PMC Funders Author Manuscripts

Europe PMC Funders Author Manuscripts

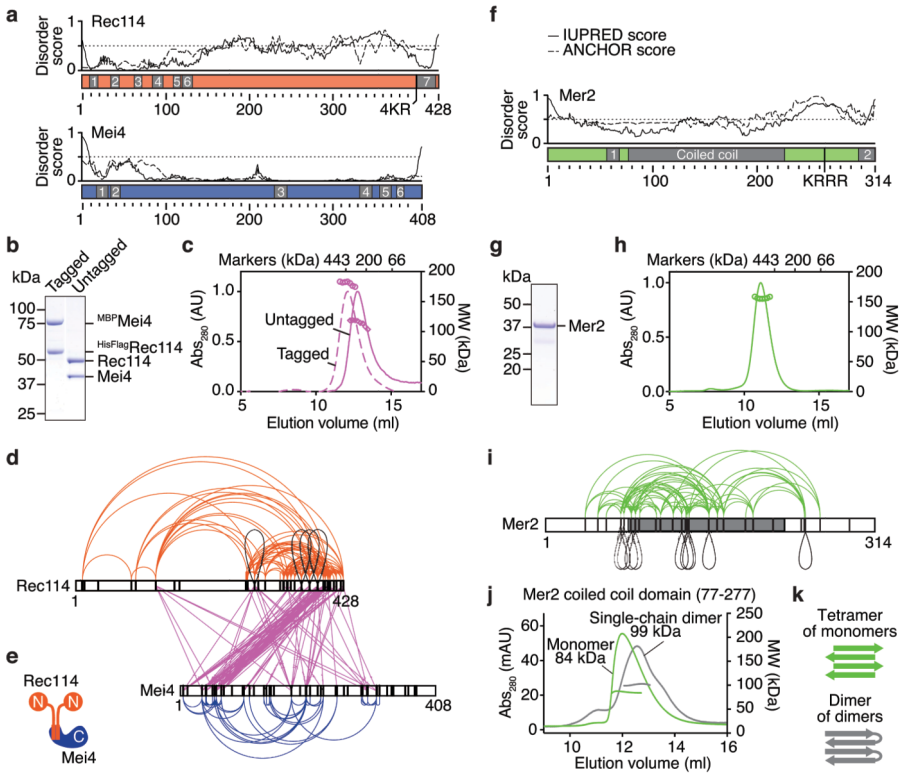

Fig. 1. Purification and subunit arrangement of the *S. cerevisiae* RMM proteins.

a. Prediction of protein disorder (IUPRED server[42]). The ANCHOR score predicts the transition from unstructured to structured depending on a binding partner. Previously identified SSMs are highlighted[23,26]. **b**. SDS-PAGE of purified tagged and untagged Rec114–Mei4 complexes. 4 μg was loaded. **c**. SEC-MALS analysis of tagged and untagged Rec114–Mei4. The traces show UV absorbance (left axis), circles are molar mass measurements across the peak (right axis). Elution positions of protein standards are marked. **d**. XL-MS analysis of Rec114–Mei4 (4812 crosslinked peptides, 258 distinct crosslinked pairs of lysines). Black loops are intermolecular self-links. Black vertical lines indicate lysines. **e**. Cartoon of the Rec114–Mei4 complex. **f**. Protein disorder prediction for Mer2. The predicted coiled coil and previously identified SSMs are highlighted[23,26]. **g**. SDS-PAGE of purified Mer2. 4 μg was loaded. **h**. SEC-MALS analysis of Mer2. **i**. XL-MS analysis of Mer2 (487 crosslinked peptides, 89 distinct crosslinked pairs of lysines). **j**. SEC-MALS analysis of the coiled coil domain of Mer2 and a single-chain dimer variant of the coiled coil domain. A tetramer of monomers and a dimer of single-chain dimers both have an expected MW of 70 kDa. The difference between the profiles of the monomer and single chain dimer can be explained by reduced degrees of freedom (tension) in the single-chain dimer and heterogeneity. **k**. Interpretive cartoon of the molecular arrangement of the coiled coil domain of Mer2. For gel source data, see Supplementary Figure 1.

Purified Rec114–Mei4 had molar masses (MW) of 180 and 114 kDa for tagged and untagged complexes, respectively, on size-exclusion chromatography with multi-angle light scattering (SEC-MALS, Fig. 1b, c). These results, plus intensities of Coomassie-stained bands and an observed 2:1 ratio of mass spectrometry spectral counts (Extended Data Fig.

1c), suggested a stoichiometry of two Rec114 subunits and one Mei4 (expected 200 and 146 kDa for tagged and untagged, respectively).

We delineated the molecular arrangement within the complexes by crosslinking plus mass spectrometry (XL-MS), observing 258 distinct pairs of crosslinked lysines (Fig. 1d & Supplementary Table 1). The Rec114 C-terminus crosslinked extensively to the Mei4 N-terminus (pink lines), implying that these are the primary interaction regions. Four inter-molecular self-links (crosslinking of two identical lysines) occurred near the C-terminal end of Rec114 (black loops in Fig. 1d), supporting the 2:1 stoichiometry and suggesting that this domain homo-dimerizes (Fig. 1e).

Truncations retaining SSM7 of Rec114 and SSMs 1 and 2 of Mei4 (Rec114$^{(375-428)}$ and Mei4$^{(1-43)}$) formed a 2:1 complex (Extended Data Fig. 1d-h). Dimerization of Rec114 C-terminal fragments did not require Mei4 (Extended Data Fig. 1h). Mutating a conserved Rec114 residue (F411A) abolished dimerization, which disrupted the interaction with Mei4 similarly to an equivalent mutation in the *Schizosaccharomyces pombe* Rec114 ortholog, Rec7 (Extended Data Fig. 1i-k)[13]. Rec114-F411A was expressed at normal levels *in vivo*, but it eliminated Rec114 foci and DSBs, leading to spore death (Extended Data Fig. 1l-o).

A homotetrameric Mer2 α-helical bundle

Mer2 has a predicted coiled coil and two SSMs[23,28], with a disordered region between the coiled coil and SSM2 (Fig. 1f). Untagged Mer2 was 156 kDa by SEC-MALS, consistent with a tetramer (143 kDa) (Fig. 1g, h), but the elution volume matched that of a considerably larger complex, suggesting an elongated shape (see marker positions in Fig. 1h).

XL-MS revealed nine intermolecular self-links (Fig. 1i). Self-links occurred along the coiled coil, consistent with parallel α-helices, but this domain also incurred long-range crosslinks. If the coiled coil forms uninterrupted helices, crosslinks further than ~ 18 amino acids cannot be explained by intra-molecular events or by intermolecular events within a parallel coiled coil. Therefore, it is likely that there are both parallel and antiparallel helices.

To address this, we first observed that the coiled-coil domain alone (residues 77-227) was still tetrameric (Fig. 1j). Next, we engineered a single-chain dimer with two copies of the coiled-coil domain separated by a 19 amino-acid linker, too short for a parallel intramolecular coiled coil. This assembled a similarly sized complex as the monomeric construct (99 vs. 84 kDa), consistent with two single-chain dimers, each folded in antiparallel (Fig. 1j, k). Alternative scenarios predict an artificially elongated single-chain dimer leading to faster elution on size exclusion, which was not observed. A plausible configuration is thus a homotetrameric alpha-helical bundle with two pairs of parallel helices arranged in antiparallel fashion (Fig. 1k).

DNA-driven condensation

Rec114, Mei4 and Mer2 orthologs in yeasts and mice form chromatin-associated foci[11,12,15,16,25,26,29,30], but the physical nature of these foci was unclear. Moreover, the

relationships between these structures, DSB formation, and the biochemical properties of Rec114, Mei4 and Mer2 were unknown.

In electrophoretic mobility shift assays, Rec114–Mei4 and Mer2 bound to 20-, 40-, and 80-bp substrates, with affinity increasing with DNA length (Fig. 2a, b, Extended Data Fig. 2a, b). Preference for longer substrates was confirmed in competition assays (Extended Data Fig. 2c, d). Protein titrations yielded well-shifts with no discrete bands and switch-like transitions from no binding to complete binding within narrow (2 to 4-fold) ranges, suggesting cooperative assembly of higher-order structures (Fig. 2a, b, Extended Data Fig. 2a, b).

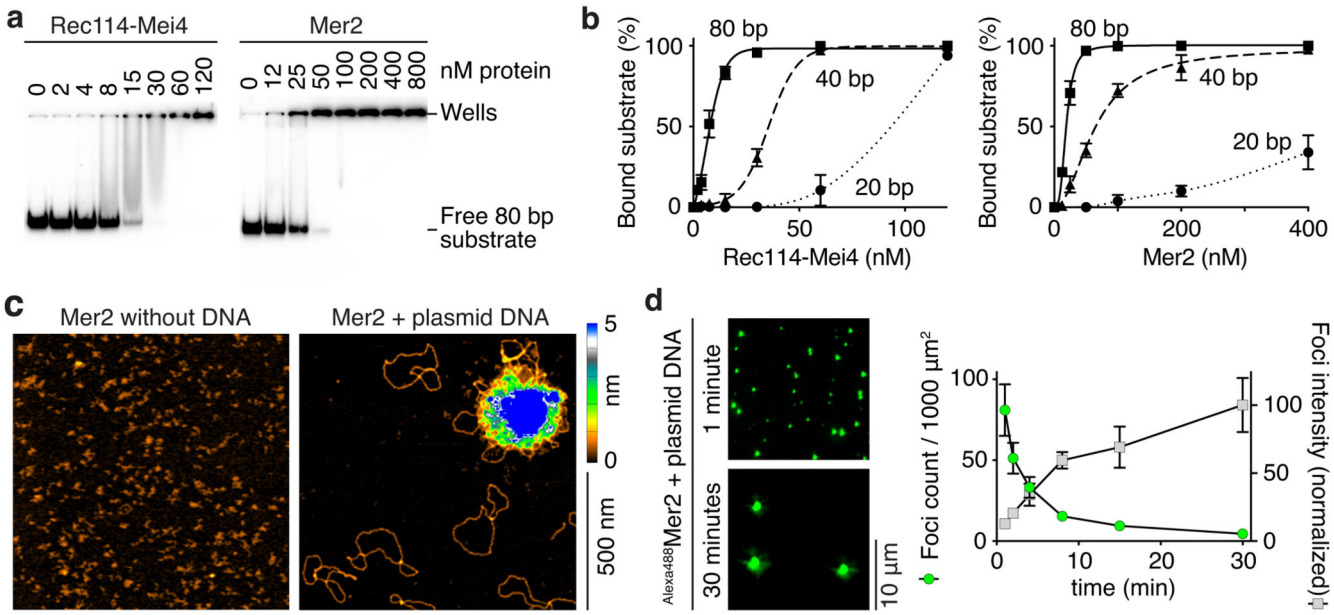

Fig. 2. Rec114–Mei4 and Mer2 form condensates on DNA.

a. Gel shift analysis of Rec114–Mei4 and Mer2 binding to 80 bp DNA substrates (see also Extended Data Fig. 2a, b). **b**. Quantification of gel-shift analyses with 20-, 40- or 80 bp substrates. Error bars are ranges from two independent experiments. Lines are sigmoidal curves fit to the data, except for the 20 bp substrate (smooth spline fits). Apparent affinities of Rec114–Mei4 are: 6 ± 1.4 nM (80 bp, mean and range); 35 ± 1.3 nM (40 bp); ≈ 80 nM (20 bp). Apparent affinities of Mer2 are: 19 ± 1.5 nM (80 bp); 64 ± 15 nM (40 bp); > 400 nM (20 bp). Here and elsewhere, concentrations for Rec114–Mei4 refer to the trimeric complex, but for Mer2 they refer to the monomer. Therefore, the complexes have comparable affinities for DNA if the quaternary units (trimers and tetramers, respectively) are considered. **c**. AFM imaging of 50 nM Mer2 in the absence (left) or presence (right) of 1 nM plasmid DNA (pUC19). **d**. Time course of the assembly of Mer2 foci in the presence of plasmid DNA. The x axis indicates the time in solution before plating, upon which DNA is immobilized to the glass slide while soluble protein is still free to diffuse. Quantification is provided of focus numbers and average focus intensity (normalized to the mean at 30 min). Error bars show mean ± SD from 8–10 fields of view (see Source Data for exact n values). For gel source data, see Supplementary Figure 1.

To directly visualize DNA-bound particles, we used atomic force microscopy (AFM). Rec114–Mei4 and Mer2 formed small, relatively homogeneous particles on the mica surface in the absence of DNA, but plasmid DNA caused Rec114–Mei4 and Mer2 to assemble large protein clusters with emanating DNA loops (Fig. 2c, Extended Data Figure 2g). Most plasmid molecules remained unbound and the surface was devoid of free protein particles, showing that clustering is extremely cooperative. From the sizes (~0.2 μm diameter for Rec114–Mei4 and ~0.4 μm for Mer2), the clusters must contain many hundreds of proteins.

Rec114–Mei4 complexes with mScarlet fused to the Rec114 N-terminus yielded bright epifluorescent foci in the presence of DNA, independent of Mg^{2+} (Extended Data Fig. 3a). eGFP-tagged Mer2 complexes also produced DNA-dependent foci in the presence of Mg^{2+}, but gave only diffuse fluorescence signal without Mg^{2+} (Extended Data Fig. 3b and 2e, f).

Properties of nucleoprotein condensates

Rec114–Mei4 and Mer2 nucleoprotein clusters resemble condensates that form intracellular membrane-less compartments and control transcription, signal transduction, stress responses, and other processes[31–36]. Biomolecular phase separation is often driven by cumulative weak interactions between multivalent components[31,35,36]. These condensates share biophysical properties: they tend to be reversible, are promoted by molecular crowding, can fuse, and may undergo sol-gel transitions over time.

We asked whether Rec114–Mei4 and Mer2 condensates display behaviors typical of phase-separated systems, using fluorophore-conjugated complexes (Extended Data Fig. 3c-f). The molecular crowding agent polyethylene glycol (5% PEG-8000) dramatically increased condensate intensity for both Rec114–Mei4 and Mer2 (Extended Data Fig. 3g, h). Protein titrations revealed complex, sometimes counter-intuitive behaviors, including a decrease in focus numbers with increasing protein concentrations. These behaviors likely reflect balances between nucleation, growth, and collapse of the condensates (see legend to Extended Data Fig. 3g, h).

Condensation was inhibited by high salt, suggesting dependency on electrostatic interactions (Extended Data Fig. 4c, e). Competition experiments revealed preferential incorporation of larger DNA molecules, consistent with multivalency of the substrate driving condensation (Extended Data Fig. 4g-h).

Pre-assembled condensates were almost completely dissolved when challenged with DNase I or 500 mM NaCl in the absence of PEG, showing that they are reversible (Extended Data Fig. 4a, b). However, in the presence of PEG, about half of the condensate-associated Rec114–Mei4 fluorescence signal resisted challenge. Reversibility of Rec114–Mei4 condensates decreased over time, accentuated by molecular crowding (Extended Data Fig. 4d). After a short assembly time, Mer2 condensates were unable to resist dissolution whether PEG was present or not, but longer incubation times with PEG allowed Mer2 as well to form resistant foci (Extended Data Fig. 4b, 4f). These results suggest that condensates of Rec114–Mei4 and, to a lesser extent, Mer2 may spontaneously mature into irreversible, perhaps gel-like, structures, as has been observed for other systems[35,37–39].

Several scenarios might account for condensate assembly, differing as to whether growth results principally from fusion of existing condensates or from incorporation of soluble protein that diffuses in and out of condensates (Extended Data Fig. 5a). To distinguish between these possibilities, we immobilized DNA at varied time points by spreading assembly reactions on glass slides. Plating should prevent focus fusion, but not exchange of condensates with soluble protein pools. Images were captured at a late time point (>1 hour), so the time variable is the period that the DNA is free in solution before constraint. If foci grow by addition from soluble protein pools, DNA immobilization should have no effect and all reactions should be identical. In contrast, if fusion drives growth, focus numbers should decrease over time while their intensities increase. The latter outcome was observed for both Rec114–Mei4 and Mer2 (Fig. 2d, Extended Data Fig. 5b). Moreover, no fluorescence recovery was seen after photobleaching of immobilized foci (Extended Data Fig. 5c). These findings thus establish that fusion can occur. However, they do not exclude exchange with soluble pools being important under other conditions, including *in vivo* (Supplementary Discussion 2).

DNA binding and RMM function

The Rec114 C-terminal domain is necessary and sufficient for DNA binding (Extended Data Fig. 6a). Alanine substitution of four basic residues in this domain yielded a Rec114–Mei4 complex (“4KR”) with reduced DNA binding (Extended Data Fig. 6b). Similarly, alanine substitutions in a conserved basic patch towards the C-terminus of Mer2 (“KRRR”) yielded a DNA-binding defective mutant (Fig. 3a, Extended Data Fig. 6c). As expected if multivalent protein-DNA interactions contribute to condensation, both the Rec114-4KR and the Mer2-KRRR mutant proteins showed strongly reduced focus formation *in vitro* (Fig. 3b, Extended Data Fig. 6d). However, fluorescently tagged Mer2-KRRR protein was incorporated into pre-assembled Mer2 condensates as efficiently as wild-type Mer2 (Extended Data Fig. 6e), indicating that the protein-protein interactions important for condensation are retained in the mutant.

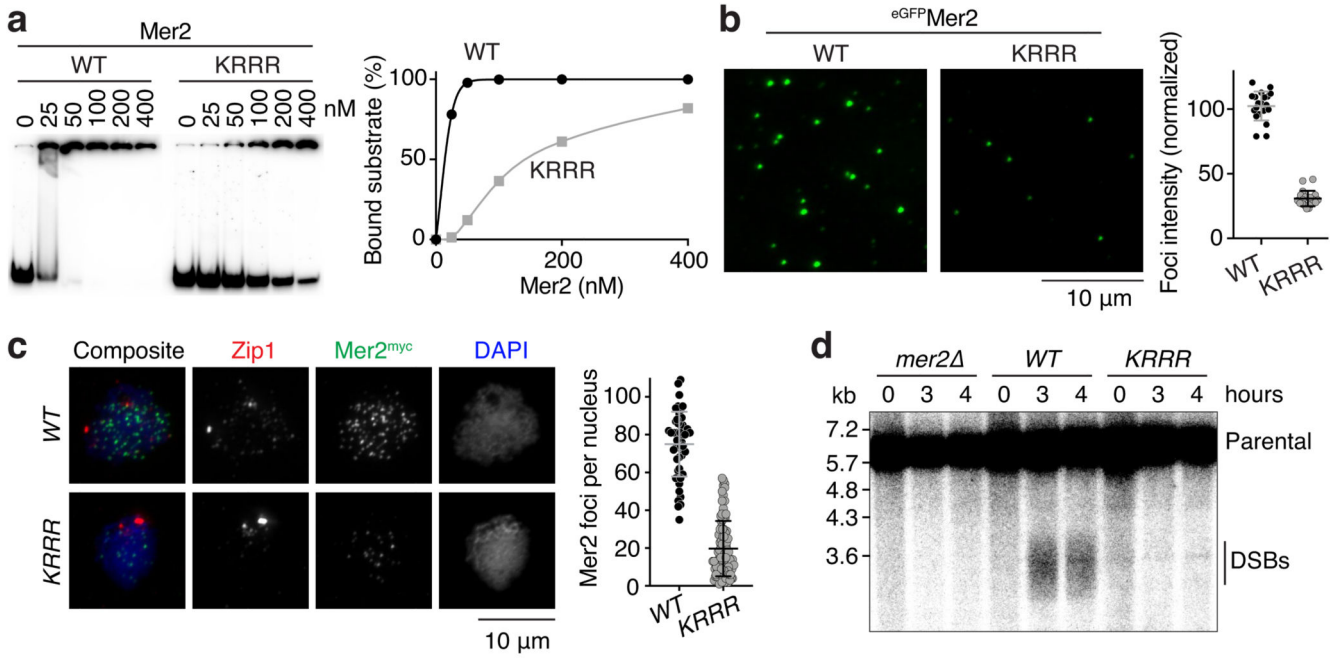

Fig. 3. DNA binding by Mer2 is important for macromolecular condensation *in vitro* and *in vivo* and for Spo11-induced break formation.

a. Gel shift assay of wild-type (WT) and mutant Mer2 complexes binding to an 80-bp DNA substrate. The Mer2-KRRR mutant has residues K265, R266, R267, and R268 mutated to alanine. Lines on the graph are a sigmoidal curve (WT) and a smooth spline (KRRR) fit to the data. **b**. Effect of the Mer2-KRRR mutation on condensation *in vitro*. Reactions included 5% PEG. Each point is the average of the intensities of foci in a field of view, normalized to the overall mean for wild type. Error bars show mean ± SD (n = 20 fields of view). **c**. Immunofluorescence on meiotic chromosome spreads for myc-tagged Mer2. The number of foci per leptotene or early zygotene cell is plotted. Error bars show mean ± SD (n = 48 and 95 cells for *WT* and *KRRR*, respectively). **d**. Southern blot analysis of meiotic DSB formation at the *CCT6* hotspot in wild type and *mer2* mutant strains. For gel source data, see Supplementary Figure 1.

In vivo, the mutant proteins formed much fewer foci than wild type upon immunofluorescent staining of chromosome spreads (Fig. 3c, Extended Data Figure 6f)[11,12,15]. This could not be attributed to protein destabilization because immunoblotting signal was not reduced compared to wild type (Extended Data Fig. 6g) and purified recombinant proteins did not show increased sensitivity to digestion with trypsin (Extended Data Fig. 6h). In fact, Mer2-KRRR mutant protein accumulated and persisted longer during meiosis (Extended Data Fig. 6i). The Mer2-KRRR protein also had faster electrophoretic mobility than wild type, probably because it failed to become phosphorylated. It therefore appears that DNA-binding is a prerequisite for Mer2 phosphorylation, which is known to promote turnover of the protein[15].

Both mutations also conferred defects in meiotic DSB formation when assayed locally by Southern blotting at a DSB hotspot (Fig. 3d, Extended Data Fig. 6j) or globally by

Europe PMC Funders Author Manuscripts

quantification of Spo11-oligo complexes (Extended Data Fig. 6k). These DSB defects caused low spore viability (Extended Data Fig. 6l). In conclusion, the DNA-binding activities of Rec114–Mei4 and Mer2 are essential for DNA-driven condensation *in vitro* and *in vivo* and for their DSB-promoting activity, suggesting in turn that condensation itself is important for these proteins' biological functions.

Comingled RMM nucleoprotein condensates

In vivo, Rec114, Mei4 and Mer2 form partially overlapping foci[11,12] and yield coincident ChIP signals[16]. We therefore tested whether they function together as joint condensates by mixing fluorescent Rec114–Mei4 and Mer2 either before or after DNA-driven condensation (Fig. 4a, b). Premixing the proteins led to joint foci with essentially perfect overlap (Fig. 4a). Colocalization was evident even with a large excess of DNA, thus joint foci were not from fortuitous overlap of independent assemblies on limiting numbers of substrate molecules (Extended Data Fig. 7a, b).

Europe PMC Funders Author Manuscripts

Europe PMC Funders Author Manuscripts

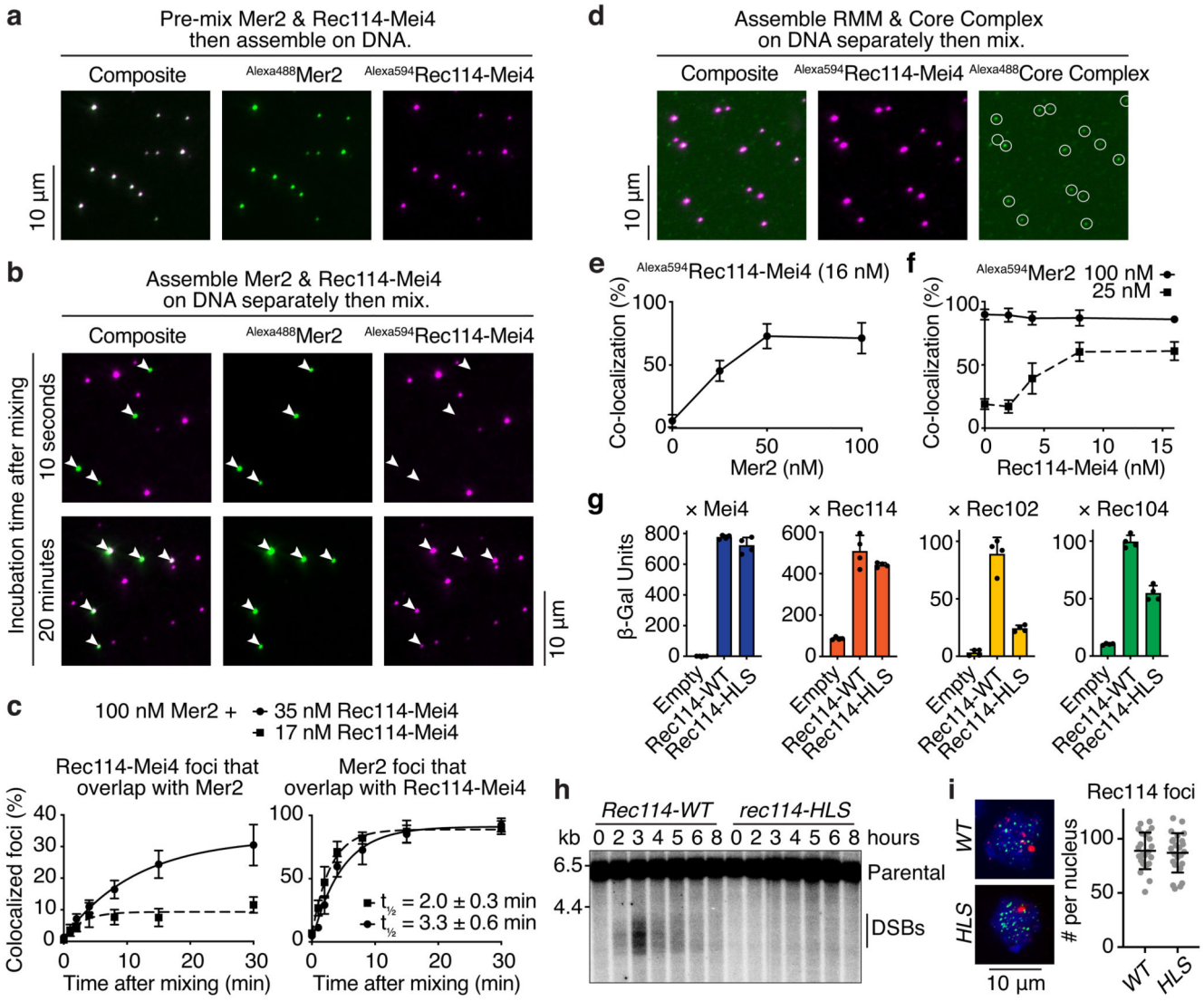

Fig. 4. Tripartite Rec114–Mei4–Mer2 nucleoprotein condensates recruit the Spo11 core complex.

a. Fluorescently labeled Rec114–Mei4 (17 nM) and Mer2 (100 nM) were mixed prior to DNA-driven condensation (for 30 minutes, 5.6 nM pUC19) and imaging by epifluorescence microscopy. **b**. Rec114–Mei4 and Mer2 nucleoprotein condensates were assembled separately for 10 minutes then mixed. After mixing, reactions contained 5.6 nM pUC19, 8.5 nM ^{Alexa594}Rec114–Mei4 and 50 nM ^{Alexa488}Mer2. Samples were dropped on a microscope slide 10 seconds (top) or 20 minutes (bottom) after mixing. White arrowheads indicate Mer2 condensates. **c**. Time course of Rec114–Mei4 and Mer2 colocalization. The time to achieve 50% of Mer2 foci overlapping with Rec114–Mei4 is indicated ($t_{½}$). Lines are one-phase association models fit to the data. Error bars show mean ± SD from 9–10 fields of view. **d**. Incorporation of Alexa488-labeled core complexes[10] into Alexa594-labeled Rec114–Mei4–Mer2 condensates. **e**. Fraction of Rec114–Mei4 foci that contained detectable core complex signal as a function of Mer2 concentration. Error bars show mean ± SD from 10 fields of view. **f**. Fraction of Mer2 foci that contained detectable core complex signal as a function of

Rec114–Mei4 concentration. Error bars show mean ± SD from 9–10 fields of view. **g**. Y2H interaction between Gal4AD-Rec114 wild type or H39A/L40A/S41A (HLS) mutant and LexA-Mei4, LexA-Rec114, LexA-Rec102, or LexA-Rec104 (mean and SD from four replicates). **h**. Southern blot analysis of meiotic DSB formation at the *CCT6* hotspot. **i**. Immunofluorescence microscopy of meiotic chromosome spreads with myc-tagged Rec114-WT and HLS mutant strains. Green, anti-myc (Rec114); red, anti-Zip1; blue, DAPI. Quantification of the number of Rec114 foci per leptotene or early zygotene cell is plotted (n = 24). Line and error bars represent mean ± SD. For gel source data, see Supplementary Figure 1. See Source Data for exact n values for panels c and f.

Next, we asked if preassembled Rec114–Mei4 and Mer2 condensates can mingle. No overlap was seen between Rec114–Mei4 and Mer2 foci when preformed nucleoprotein condensates were mixed and then immediately plated (Fig. 4b, top). In contrast, when the mixtures were incubated for 20 minutes prior to plating, all of the Mer2 condensates overlapped with a Rec114–Mei4 focus (Fig. 4b, bottom). The lack of overlap in samples that were plated immediately rules out the joint foci arising via a pool of soluble protein under these conditions, so we infer that existing condensates can fuse.

To further test this, we performed a time course experiment with different concentrations of Rec114–Mei4 (17 and 35 nM) (Fig. 4c). As shown above, the lower concentration yields more foci (Extended Data Fig. 3g). If the likelihood of cluster fusion reflects contact probability, the rate of forming joint foci would be expected to be higher with the lower concentration of Rec114–Mei4. This was indeed the case: the halftime for detecting joint foci was 2.0 ± 0.3 min for 17 nM vs. 3.3 ± 0.6 min for 35 nM (Fig. 4c, right panel).

We also asked whether soluble protein can be recruited into condensates. Here, Rec114–Mei4 or Mer2 condensates were assembled, then the other protein was added in solution and the mixtures were immediately plated to prevent subsequent fusion. Preassembled Rec114–Mei4 foci incorporated Mer2 and vice versa (Extended Data Fig. 7c), showing that condensates provide nucleation sites for the partner complexes.

Interaction of Mer2 and Rec114–Mei4 complexes within nucleoprotein condensates may account for their interactions in immunoprecipitation and Y2H experiments[11–14,17] despite not forming a stable tripartite complex (Extended Data Fig. 1a, b). We observed weak interactions between recombinant proteins by affinity pulldown (Extended Data Fig. 7d). Moreover, XL-MS applied to mixtures of both complexes in the presence of DNA yielded numerous crosslinks between the Rec114 C-terminal domain and the coiled coil region of Mer2, and between Mei4 and Mer2 at multiple positions along their lengths (Extended Data Fig. 7e).

RMM condensates recruit Spo11

When fluorescently labeled Spo11 core complexes bound to DNA were mixed with preassembled RMM-DNA condensates, core complex signal overlapped with RMM foci (Fig. 4d). Recruitment of the core complex depended on Mer2 (Fig. 4e, Extended Data Fig

8a). Rec114-Mei4 was also required when Mer2 was present at low concentration (25 nM), but was dispensable at high Mer2 concentration (100 nM) (Fig. 4f, Extended Data Fig. 8b).

Rec114 interacts with Rec102 and Rec104 in Y2H assays[12,17]. Consistent with these interactions mediating recruitment of core complexes to condensates, an excess of Rec102–Rec104 subcomplexes was able to outcompete the full core complex (Extended Data Fig. 8c, d).

We mapped the core complex interacting domain of Rec114 by Y2H truncation analysis (Extended Data Fig. 8e). Deleting ~50 amino acids from either the N or C termini of Rec114 abolished interaction with both Rec102 and Rec104, but deleting the disordered region did not (residues 152-377, see Fig. 1a). Altering conserved residues in the N-terminal PH domain identified a mutation (HLS, H39A/L40A/S41A) that specifically reduced interactions with Rec102 and Rec104 but did not affect the interaction with Mei4 or wild-type Rec114 (Fig. 4g), or the ability to make comingled RMM condensates *in vitro* (Extended Data Fig. 8f). The *rec114-HLS* mutant was defective for DSB formation (Fig. 4h) and gave inviable spores (Extended Data Fig. 8g) despite the mutant protein being expressed at normal levels (Extended Data Fig. 8h) and forming normal-looking chromatin-associated foci (Fig. 4i).

These data are consistent with the idea that the core complex is recruited to Rec114–Mei4–Mer2 condensates through at least two sets of interactions: one that depends on Mer2 and another involving contacts between the Rec114 PH domain and both Rec102 and Rec104.

Discussion

We have shown that Rec114–Mei4 and Mer2 form separate subcomplexes *in vitro* that each bind DNA with high cooperativity and assemble micrometer-scale nucleoprotein super-complexes reminiscent of biomolecular condensates that control a variety of processes[31–36]. These assemblies are reversible, can fuse both homotypically and heterotypically, and depend on multivalent protein-DNA and protein-protein interactions (Supplementary Discussion 3). Because mutations that disrupt condensate formation also disrupt DSB formation *in vivo*, it appears that DNA-driven condensation is an important aspect of recombination initiation.

Meiotic chromosomes form chromatin loops extending from a linear protein axis and it is thought that the DSB machinery assembled on axes captures and breaks loop DNA[5,16]. We propose that recruitment of Spo11 and regulatory components to RMM clusters forms the basis of this tethered loop-axis configuration (Extended Data Fig. 9a and Supplementary Discussion 4).

This model has important implications. First, each cluster likely recruits multiple core complexes, so it may explain how core complexes can be induced to dimerize[10] and how Spo11 can sometimes cut the same chromatid more than once[40,41]. RMM condensates may also provide platforms that display co-oriented arrays of Spo11 complexes, which could account for observed 10-bp periodicity in the spacing between Spo11 cuts[41] (Extended Data Fig. 9a and Supplementary Discussion 4).

Second, RMM condensates may explain two previously unclear aspects of DSB patterning: hotspot competition, where strong hotspots reduce activity of neighboring hotspots, and DSB interference, in which the DSB-responsive kinase Tel1 inhibits additional DSBs near an existing DSB[4] (Extended Data Fig. 9b and Supplementary Discussion 5). Hotspot competition could arise if nucleation of a condensate plus highly cooperative assembly locally depletes Rec114–Mei4 and Mer2 proteins, reducing the probability of another nucleation event. After a DSB is made, Tel1 may suppress additional DSBs nearby by acting both within and between adjacent condensates.

Third, the condensates may regulate DSB repair, for example by tethering and controlling the broken DNA ends and/or by nucleating formation of the recombination nodules where repair takes place (Extended Data Fig. 9c and Supplementary Discussion 6).

In summary, our findings reveal how the DSB machinery self-organizes into punctate clusters that integrate DNA breakage with the loop-axis structure of chromosomes and that may thereby control DSB number, location and timing and coordinate DSB formation with downstream repair. DNA-driven RMM condensates thus provide insight into how cells mitigate risks from the potentially dangerous generation of programmed DNA breaks during meiosis.

Methods

Preparation of expression vectors

Oligonucleotides (oligos) used in this study were purchased from Integrated DNA Technologies. The sequence of the oligos is listed in Supplementary Table 2. Plasmids are listed in Supplementary Table 3.

Separate exons of *S. cerevisiae REC114*, *MEI4* and *MER2* were amplified from genomic DNA of the SK1 strain and assembled by in-fusion cloning to yield intron-less pFastbac1-derived expression vectors pCCB649, pCCB652 and pCCB681, respectively. Primers for *REC114* were: cb906 and cb907 (exon 1), and cb908 and cb909 (exon 2). Primers for *MEI4* were: cb910 and cb911 (exon 1), and cb912 and 913 (exon 2). Primers for *MER2* were: cb978 and cb979 (exon 1), and cb980 and cb981 (exon 2). The genes were subcloned into pFastBac-HTb-Flag to generate N-terminally HisFlag-tagged expression vectors for ^{HisFlag}Rec114 (pCCB650), Mei4 (pCCB653) and Mer2 (pCCB682). MBP was subcloned into the untagged vectors, to yield expression vectors for ^{MBP}Rec114 (pCCB651) and ^{MBP}Mei4 (pCCB654), ^{MBP}Mer2 (pCCB683).

To generate untagged Rec114–Mei4, the cleavage sequence for the TEV protease was introduced between the affinity tag and the sequence coding for Rec114 and Mei4 by inverse PCR and self-ligation using templates pCCB650 (primers cb1283 and cb1284), and pCCB654 (primers cb1287 and cb1288), to yield vectors pCCB789 ($^{HisFlag\text{-}TEV}$Rec114) and pCCB791 ($^{MBP\text{-}TEV}$Mei4), respectively. The mScarlet fluorophore was amplified from a synthetic gene codon-optimized for mammalian expression (gift from Soonjoung Kim, MSKCC) with primers cb1279 and cb1280 and cloned into the BamHI site of pCCB650 to yield pCCB786 ($^{HisFlag\text{-}mScarlet}$Rec114). A TEV cleavage site was further introduced

between the affinity tag and the fluorophore by inverse PCR and self-ligation using template pCCB786 and primers cb1285 and cb1286 to yield pCCB790 ($^{HisFlag\text{-}TEV\text{-}mScarlet}$Rec114). The Rec114-R395A/K396A/K399A/K400A (4KR) mutant was generated by inverse-PCR and self-ligation of pCCB789 and pCCB790 with primers cb1332 and cb1334 to yield pCCB848 ($^{HisFlag\text{-}TEV}$Rec114-4KR), pCCB849 ($^{HisFlag\text{-}TEV\text{-}mScarlet}$Rec114-4KR).

To generate a vector for Mer2 expression in *E. coli*, *MER2* was amplified from pCCB681 using primers cb1161 and cb1162 and cloned into the BamHI site of pSMT3 to yield pCCB750 (^{SUMO}Mer2). eGFP-tagged Mer2 was generated by PCR amplification of eGFP using primers cb1259 and cb1260 and in-fusion cloning in the BamHI site of pCCB750 to yield pCCB777 ($^{SUMO\text{-}eGFP}$Mer2). The Mer2-K265A/R266A/R267A/R268A (KRRR) mutation was generated by QuikChange mutagenesis using primers cb1186 and cb1187 pf pCCB750 and pCCB777 to yield pCCB779 (^{SUMO}Mer2-KRRR) and pCCB783 ($^{SUMO\text{-}eGFP}$Mer2-KRRR), respectively.

Full-length Rec114 and Mei4 were amplified from pCCB649 and pCCB650 using primers sp16 and sp17, and sp25 and sp26, respectively and cloned into the pETDuet-1 vector by in-fusion cloning to yield pSP34. A SUMO tag was introduced at the N-terminus of Rec114 by PCR amplification of the pSMT3 vector with primers cb1172 and cb1180 and In-Fusion cloning within the Nco1 and BamHI fragment of pSP34 to yield pSP53. Truncations were obtained from this construct by inverse PCR and self-ligation.

Expression vectors for purification of the core complex and Rec102–Rec104 from baculovirus-infected insect cells are described separately[10].

Expression and purification of recombinant proteins

Viruses were produced by a Bac-to-Bac Baculovirus Expression System (Invitrogen) following the manufacturer's instructions. 2×10^9 *Spodoptera frugiperda* Sf9 cells were infected with combinations of viruses at a multiplicity of infection (MOI) of 2.5 each. Authentication of Sf9 cells and tests for mycoplasma contamination were conducted by the supplier (Gibco, Thermo Fisher 11496015). Expression of ^{HisFlag}Rec114-^{MBP}Mei4 used viruses generated from pCCB650 and pCCB654, untagged Rec114–Mei4 used viruses generated from pCCB789 and pCCB791, and fluorescently tagged ^{mScarlet}Rec114–Mei4 used viruses generated from pCCB790 and pCCB791. After 62 h infection, cells were harvested, washed with phosphate buffer saline (PBS), frozen in dry ice and kept at -80 °C until use. All the purification steps were carried out at 0–4 °C. Cell pellets were resuspended in 4 volumes of lysis buffer (25 mM HEPES-NaOH pH 7.5, 500 mM NaCl, 0.1 mM DTT, 20 mM imidazole, 1x Complete protease inhibitor tablet (Roche) and 0.1 mM phenylmethanesulfonyl fluoride (PMSF)). Cells were lysed by sonication and centrifuged at 43,000 g for 30 min. The cleared extract was loaded onto 1 ml pre-equilibrated NiNTA resin (Qiagen). The column was washed extensively with Nickel buffer (25 mM HEPES-NaOH pH 7.5, 500 mM NaCl, 10% glycerol, 0.1 mM DTT, 20 mM imidazole, 0.1 mM PMSF). The tagged complexes were then eluted in Nickel buffer containing 250 mM imidazole. The complexes were further purified on amylose resin (NEB). Fractions containing protein were pooled and diluted in 3 volumes of Amylose buffer (25 mM HEPES-NaOH pH 7.5, 500 mM NaCl, 10% glycerol, 2 mM DTT, 5 mM EDTA). Next, the complexes were bound to 1 ml of

the Amylose resin in a poly-prep chromatography column (Bio-Rad) and the resin was washed extensively. Complexes were eluted from amylose resin with buffer containing 10 mM maltose. Fractions containing protein were pooled and loaded on a Superdex 200 column preequilibrated with Amylose buffer. For untagged or mScarlet-tagged complexes, samples were treated with an excess of TEV protease prior to gel filtration. For fluorescently labeled complexes, labeling was performed using Alexa Fluor 594 (Invitrogen #A10239), which has a succinimidyl ester moiety that reacts with primary amines. After 1 hour conjugation at room temperature, complexes were purified by gel filtration. Fractions containing protein were concentrated in 50 kDa cutoff Amicon centrifugal filters (Millipore). Aliquots were frozen in dry ice and stored at -80 °C.

For expression of recombinant proteins in *E. coli*, expression vectors were transformed in BL21 DE3 cells and plated on LB plates containing the appropriate antibiotic. Cells were then cultured in liquid medium at 37 °C to OD_{600} = 0.6. For Mer2 proteins and variants, expression was carried out at 30 °C for 3 hours with 1 mM IPTG. For Rec114–Mei4 truncations, expression was carried out at 16 °C overnight with 0.2 mM IPTG. Cells were resuspended in Nickel buffer (25 mM HEPES-NaOH pH 7.5, 500 mM NaCl, 10% glycerol, 0.1 mM DTT, 20 mM imidazole, 0.1 mM PMSF) and frozen dropwise in liquid nitrogen and kept at -80 °C until use. All the purification steps were carried out at 0–4 °C. Cells were lysed using a French press and centrifuged at 43,000 g for 30 min. The cleared extract was loaded onto 1 ml pre-equilibrated NiNTA resin (Qiagen). The column was washed extensively with Nickel buffer then eluted in buffer containing 250 mM imidazole. The 6His-SUMO tag was cleaved with Ulp1 during overnight dialysis in gel filtration buffer (25 mM HEPES-NaOH pH 7.5, 300 mM NaCl, 10% glycerol, 40 mM imidazole, 1 mM DTT, 5 mM EDTA). The sample was then loaded on a second Nickel column to remove 6His-SUMO and Ulp1. The flow-through was then loaded on a Superdex 200 column preequilibrated with gel filtration buffer. For Mer2 complexes labeled with Alexa Fluor 488 (Invitrogen #A10235), fluorophore conjugation was performed at room temperature for 1 hour prior to gel filtration. Alexa Fluor 488 has a tetrafluorophenyl ester moiety that reacts with primary amines. After gel filtration, fractions containing protein were concentrated in 10 kDa cutoff Amicon centrifugal filters (Millipore). Aliquots were frozen in dry ice and stored at -80 °C.

Purification of $Alexa^{488}$-labeled Spo11 core complexes was achieved essentially as described[10], except with an additional fluorophore conjugation step prior to gel filtration. Briefly, $Spo11^{HisFlag}$:Ski8:Rec102:Rec104 were expressed in *Spodoptera frugiperda* Sf9 cells by co-infection with a combination of baculoviruses coding for individual subunits. Cells were harvested 62 hours after infection and the complexes purified by sequential affinity chromatography on NiNTA resin and anti-Flag resin. Complexes were dialyzed in buffer containing 25 mM HEPES-NaOH pH 7.5, 500 mM NaCl, 10% glycerol, 2 mM DTT, 5 mM EDTA, then conjugated to Alexa Fluor 488 (Invitrogen #A10235) by 1-hour incubation at room temperature and purified by size exclusion chromatography on a Superdex 200 column. Finally, fractions containing protein were concentrated and aliquots stored at -80 °C. Rec102–Rec104 complexes were purified by co-infection of Sf9 cells with viruses expressing ^{MBP}Rec102 and $Rec104^{HisFlag}$. Complexes were purified by sequential

affinity chromatography on NiNTA resin and amylose resin, using the same procedure as for the core complex[10].

SEC-MALS

Light scattering data in Fig. 1c, h were collected using a Superdex 200, 10/300, HR Size Exclusion Chromatography (SEC) column (GE Healthcare, Piscataway, NJ), connected to High Performance Liquid Chromatography System (HPLC), Agilent 1200, (Agilent Technologies, Wilmington, DE) equipped with an autosampler. The elution from SEC was monitored by a photodiode array (PDA) UV/VIS detector (Agilent Technologies, Wilmington, DE), differential refractometer (OPTI-Lab rEx Wyatt Corp., Santa Barbara, CA), static and dynamic, multiangle laser light scattering (LS) detector (HELEOS II with QELS capability, Wyatt Corp., Santa Barbara, CA). The SEC-UV/LS/RI system was equilibrated in buffer 25 mM Hepes pH 7.5, 500 mM NaCl, 10 % glycerol, 2 mM EDTA at the flow rate of 0.5 ml/min or 1.0 ml/min. Two software packages were used for data collection and analysis: the Chemstation software (version B.04.03-SP1, Agilent Technologies, Wilmington, DE) controlled the HPLC operation and data collection from the multi-wavelength UV/VIS detector, while the ASTRA V software (Wyatt Corp., Santa Barbara, CA) collected data from the refractive index detector, the light scattering detectors, and recorded the UV trace at 280 nm sent from the PDA detector. The weight average molecular masses were determined across the entire elution profile in intervals of 1 sec from static LS measurement using ASTRA software.

All other SEC-MALS experiments were performed by an Äkta-MALS system. Proteins (500 µl) were loaded on Superdex 75 10/300 GL or Superdex 200 10/300 GL columns (GE Healthcare) and eluted with buffer 20 mM Tris pH 7.5, 300 mM NaCl, 2 mM DTT at a flow rate of 0.3 ml/min. The light scattering was monitored by a miniDAWN TREOS system (Wyatt Technologies) and concentration was measured by an Optilab T-rEX differential refractometer (Wyatt Technologies).

Crosslinking and mass spectrometry

For crosslinking of purified proteins, ~20–50 µg of ^{HisFlag}Rec114–^{MBP}Mei4 or ^{HisFlag}Mer2 complexes were incubated in 50–100 µl reactions in the presence of 2 mM disuccinimidyl suberate (DSS) in buffer containing 25 mM HEPES-NaOH pH 7.5, 500 mM NaCl, 10% glycerol, 2 mM DTT, 5 mM EDTA. For crosslinking of condensates, 900 µl reactions containing 30 µg of ^{HisFlag}Rec114–^{MBP}Mei4 and 20 µg of Mer2 complexes in 20 mM HEPES-NaOH pH 7.5, 100 mM NaCl, 5% glycerol, 5 mM $MgCl_2$ and 100 ng/µl pUC19 were incubated at 30 °C prior to the addition of 2 mM DSS. After 10 minutes crosslinking at 30 °C, reactions were quenched with 100 mM Tris-HCl pH 7.5. Crosslinked proteins were separated by SDS-polyacrylamide gel electrophoresis and stained with SimplyBlue (Invitrogen). Protein bands were excised and digested *in situ* with trypsin as described[43]. The tryptic peptides were purified using a 2-µl bed volume of Poros 50 R2 (Applied Biosystems) reverse-phase beads packed in Eppendorf gel-loading tips[44]. The digested peptides were diluted in 0.1% formic acid, and each sample was analyzed separately by microcapillary LC with tandem MS by using the NanoAcquity system (Waters) with a 100 µm inner diameter × 10 cm length C18 column (1.7 µm BEH130; Waters) configured with a

Europe PMC Funders Author Manuscripts

180 μm × 2 cm trap column coupled to a Q-Exactive Plus mass spectrometer (Thermo Fisher Scientific). A proxeon nanoelectrospray source set at 1800 V and a 75 μm (with 10 μm orifice) fused silica nano-electrospray needle (New Objective, Woburn, MA) was used to complete the interface. 1 μl of sample was loaded onto the trap column, washed with 3x loop volume of buffer A (0.1% formic acid) and the flow was reversed through the trap column and the peptides eluted with a 1-50% acetonitrile (with 0.1% formic acid) gradient over 50 min at a flow rate of 300 nl/min over the analytical column. The QE Plus was operated in automatic, data-dependent MS/MS acquisition mode with one MS full scan (370–1700 m/z) at 70,000 mass resolution and up to ten concurrent MS/MS scans for the ten most intense peaks selected from each survey scan. Survey scans were acquired in profile mode and MS/MS scans were acquired in centroid mode at 17500 resolution and isolation window of 1.5 amu. AGC was set to 1×10^6 for MS1 and 5×10^5 and 100 ms maximum IT for MS2. Charge exclusion of 1, 2 and greater than 8 enabled with dynamic exclusion of 15 s. To analyze the cross-linked peptides we used pLink[45]. The raw MS data was analyzed using pLink search with the following parameters: precursor mass tolerance 50 p.p.m., fragment mass tolerance 10 p.p.m., cross-linker DSS (cross-linking sites K and protein N terminus), xlink mass-shift 138.068, monolink mass-shift 156.079, fixed modification C 57.02146, variable modification oxidized methionine, deamidation N,Q, protein N-acetyl, peptide length minimum 4 amino acids and maximum 100 amino acids per chain, peptide mass minimum 400 and maximum 10,000 Da per chain, enzyme trypsin, two missed cleavage sites per chain (four per cross-link). The data were imported on the xiNET online tool to generate crosslinking maps[46]. All identified crosslinks can be found in **Data File 1**.

To estimate the ratio of Rec114 and Mei4 by mass spectrometry, 10 μg of ^{HisFlag}Rec114–^{MBP}Mei4 were digested with trypsin, analyzed by tandem MS as described above, and spectral counts of the two proteins were compared, omitting the tags. Rec114 and Mei4 have similar lengths (428 and 408 amino acids, respectively), and similar numbers of K and R residues (56 and 66 respectively). The average and median trypic peptide length is 7.6 and 5 for Rec114, and 6.1 and 4 for Mei4. The .raw files were converted to .mgf and searched by Mascot (Matrix Science, version 2.6.100) using the Fasta formatted Swissprot reviewed database (downloaded July 5, 2017 from www.UniProt.org) and the Fasta formatted Rec114 and Mei4 sequence. The search parameters were as follows: (i) two missed cleavage tryptic sites were allowed; (ii) precursor ion mass tolerance 10 ppm; (iii) fragment ion mass tolerance 0.08 Da (monoisotopic); and (iv) fixed modification of carbamidomethyl of cysteine; (v) variable protein modifications were allowed for methionine oxidation, deamidation on NQ, protein N-terminal acetylation, and phospho STY. Scaffold (version Scaffold_4.8.4, Proteome Software Inc., Portland, OR) was used to validate MS/MS based peptide and protein identifications. Peptide identifications were accepted if they could be established at greater than 70% probability to achieve an FDR less than 1% by the Scaffold Local FDR algorithm. Protein identifications were accepted if they could be established at greater than 6% probability to achieve an FDR less than 1% and contained at least 2 identified peptides. Protein probabilities were assigned by the Protein Prophet algorithm[47]. Proteins that contained similar peptides and could not be differentiated based on MS/MS analysis alone were grouped to satisfy the principles of parsimony. Proteins sharing significant peptide evidence were grouped into clusters.

AFM imaging

For AFM imaging of Rec114–Mei4 or Mer2 bound to plasmid DNA, protein complexes were diluted to the indicated concentration (12–50 nM) in the presence of 1 nM supercoiled pUC19 in 25 mM HEPES-NaOH pH 6.8, 5 mM $MgCl_2$, 50 mM NaCl, 10% glycerol. Complexes were assembled at 30 °C for 30 minutes. A volume of 40 μl of the protein-DNA binding reaction was deposited onto freshly cleaved mica (SP1) for 2 minutes. The sample was rinsed with 10 ml ultrapure deionized water and the surface was dried using a stream of nitrogen. AFM images were captured using an Asylum Research MFP-3D-BIO (Oxford Instruments) microscope in tapping mode at room temperature. An Olympus AC240TS-R3 AFM probe with resonance frequencies of approximately 70 kHz and spring constant of approximately 1.7 N/m was used for imaging. Images were collected at a speed of 0.5–1 Hz with an image size of 2 μm at 2048 × 2048 pixel resolution.

DNA substrates and gel shift assays

Short linear DNA substrates were generated by annealing complementary oligos (sequences listed in Supplementary Table 2). The substrates were the following (with oligo names in parentheses): dsDNA20 (cb939 & cb940), dsDNA40 (cb922 & cb935), dsDNA80 (cb95 & cb100). The 80 nt oligos were first purified on 10% polyacrylamide-urea gels. Oligos were subsequently mixed in equimolar concentrations (10 μM) in STE (100 mM NaCl, 10 mM Tris-HCl pH 8, 1 mM EDTA), heated and slowly cooled on a PCR thermocycler (98°C for 3 min, 75°C for 1 h, 65°C for 1 h, 37°C for 30 min, 25°C for 10 min). For radioactive labeling, $1/20^{th}$ of the annealed substrates were 5 -end-labeled with [γ-^{32}P]-ATP (Perkin Elmer) and T4 polynucleotide kinase (New England Biolabs). Labeled and unlabeled substrates were purified by native polyacrylamide gel electrophoresis. Larger linear substrates were prepared by PCR amplification of a 9.6-kb template derived from pUC19 (pDR470). Substrates were as follows: 100 bp (cb343 & cb1339), 1000 bp (cb342 & cb343), 9.6 kb (cb1175 & cb1177 or cb343 & cb1338). Fluorescently labeled substrates were prepared by PCR amplification of pDR470 as follows: Cy3-100bp (cb1330 & cb1339), Cy3-9.6kb (cb1330 & cb1338), Cy5-100bp (cb1331 & cb1339), Cy5-9.6kb (cb1331 & cb1338). PCR products were purified by agarose gel electrophoresis.

Short double-stranded DNA substrates were prepared by annealing the following complementary oligonucleotides: 20 bp (cb939 & cb940), 40 bp (cb922 & cb935), 80 bp (cb95 & cb100). Substrates were labeled with [γ-^{32}P]-ATP by polynucleotide kinase and gel purified. Binding reactions (20 μl) were carried out in 25 mM Tris-HCl pH 7.5, 7.5% glycerol, 100 mM NaCl, 2 mM DTT and 1 mg/ml BSA with 1 mM EDTA or 5 mM $MgCl_2$, when indicated. Unless stated otherwise, reactions contained 2 nM pUC19 or 0.5 nM radiolabeled substrate and the indicated concentration of protein. Concentrations for Rec114–Mei4 were calculated based on a 2:1 stoichiometry. For Mer2, the concentrations are expressed as monomers. Complexes were assembled for 30 minutes at 30 °C and separated by gel electrophoresis. For plasmid substrates, binding reactions were loaded on a 0.5% agarose (Gold) gel in 40 mM Tris-acetate buffer supplemented with 1 mM EDTA or 5 mM $MgCl_2$, as indicated, at 50 V for 2.5 hours. Gels were stained with ethidium bromide and scanned using a ChemiDoc Imaging System (Bio-Rad). For short substrates, binding

reactions were separated on 8% TAE-polyacrylamide gels at 200 V for 2 hours, gels were dried and imaged by autoradiography.

In vitro condensation assays

DNA-driven condensation reactions were assembled as follows: RMM proteins were first diluted to 5 μl in storage buffer adjusted to a final salt concentration of 360 mM NaCl. After 5 minutes at room temperature, condensation was induced by 3-fold dilution in reaction buffer containing DNA and no salt, to reach final 15-μl reactions that contained 25 mM Tris-HCl pH 7.5, 5% glycerol, 120 mM NaCl, 2 mM DTT, 1 mg/ml BSA, 5 mM $MgCl_2$, 5% PEG 8000, unless indicated otherwise. A typical binding reaction contained 150 ng supercoiled pUC19 (5.7 nM), 50–200 nM Mer2 (^{Alexa488}Mer2 or ^{eGFP}Mer2) and/or 8–35 nM Rec114–Mei4 (^{Alexa594}Rec114–Mei4 or ^{mScarlet}Rec114–Mei4). For experiments with core complexes, binding reactions containing 25 nM ^{Alexa488}Core complex with or without 200 nM ^{MBP}Rec102–Rec104^{HisFlag} competitor were assembled for 10 minutes, then mixed with an equal volume of reactions containing Rec114–Mei4–Mer2 condensates. After 30 minutes incubation at 30 °C with occasional mixing, 4 μl were dropped on a microscope slide and covered with a coverslip. Images were captured on a Zeiss Axio Observer Z1 Marianas Workstation with a 100×/1.4 NA oil immersion objective. Marianas Slidebook (Intelligent Imaging Innovations) software was used for acquisition. Images were analyzed with Image J using a custom-made script. Briefly, 129.24 × 129.24 μm (2048 × 2048 pixels) images were thresholded using the mean intensity of the background plus 3 times the standard deviation of the background. For experiments where the number of foci is compared between wild-type and mutant proteins or between reactions with and without Mg^{2+}, a fixed threshold was applied. Masked foci were counted and the intensity inside the foci mask was integrated. Datapoints represent averages of at least 8–10 images per sample. Data were analyzed using Graphpad Prism 8.

Yeast strains and targeting vectors

Yeast strains were from the SK1 background. All strains used in this study are listed in Supplementary Table 4.

Strains that have endogenous *MER2* replaced by *kanMX4* cassette (SKY1524 and SKY1525) were described[15]. *MER2myc5::URA3* was inserted at the *mer2Δ::kanMX4* locus by EcoRI linearization of pRS306-derived pSK351 (WT) and pJX005 (KRRR) and transformation into SKY1524 and SKY1525 to yield SKY1560 and SKY1695 (WT), and SKY6411 and SKY6413 (KRRR). Integration of the vectors was confirmed by PCR.

Strains that have endogenous *REC114* replaced by the *kanMX4* cassette (SKY865 and SKY866) were described[12]. Tagged and untagged *REC114* alleles were generated by transformation of SKY865 and SKY866 with AflII-digested plasmids pRS305-derived targeting vectors. Plasmids and resultant strains were as follows: *REC114-8myc* (pSK591, SKY6749 & SKY6750), *REC114* (pSK592, SKY6562 & SKY6563), *rec114(F411A)-8myc* (pCCB857, SKY6889 & SKY6890), r*ec114(F411A)* (pCCB856, SKY6885 & SKY6886), *rec114(4KR)-8myc* (pCCB851, SKY6859 & SKY6860), *rec114(HLS)-8myc* (pSP113, SKY6797 & SKY6798).

Y2H vectors for wild-type DSB proteins were described previously[12,17]. pACT2-derived plasmids carry the *LEU2* marker and express the Gal4-activator domain. pCA1-derived plasmids carry the *TRP1* marker and express the DNA-binding domain of LexA. The vectors used here are as follows: pACT2-Rec114 (pSK304) encodes for Gal4AD-Rec114, pCA1-Mei4 (pSK281) encodes for LexA-Mei4, pCA1-Rec102 (pSK282) encodes for LexA-Rec102, pCA1-Rec104 (pSK283) encodes LexA-Rec104. Gal4AD empty vector control (pACT2) is pSK276. Y2H vectors for Rec114 truncations were generated by inverse PCR and self-ligation of the full-length construct pSK304. Plasmid numbers are as follows: Rec114(152-277) (pSP9), Rec114(del1-50&152-277) (pSP1), Rec114(del101-277) (pSP3), Rec114(del152-377) (pSP6). Rec114(53-428) and Rec114(1-377) were reported[12]. Point mutants were made by QuikChange mutagenesis and were as follows: Rec114-HLS (pSP25), Rec114-F411A (pCCB858).

Immunofluorescence of yeast nuclei spreads

Diploid strains were cultured overnight in YPD (1% yeast extract, 2% peptone, 2% dextrose), followed by 13.5–14 hours in YPA (1% yeast extract, 2% peptone, 2% potassium acetate (KOAc)). Meiosis was induced by transfer to 2% KOAc. After 3.5 hours, cells were harvested, washed with H_2O, resuspended in 1 M sorbitol, 1x PBS pH 7, 10 mM DTT, 0.5 mg/ml zymolyase 20T, and incubated for 30 minutes at 30 °C with gentle shaking. Spheroplasts were collected by centrifugation at 1500 g, washed in ice-cold 100 mM MES, 1 M sorbitol, spun down, then lysed in ice-cold 20 mM MES, 3 % paraformaldehyde and spread on a microscope slide for 1 hour. Slides were washed three times with 1 ml 0.4% PhotoFlo 200 solution (Kodak), air dried and stored at -20 °C. Slides were blocked with 90% FBS, 1 × PBS for 1 hour at room temperature in a humid chamber, then incubated with primary antibody diluted in 3% BSA, 1 × PBS in a humid chamber at 4 °C. After 3 × 5-minute washes with 1 × PBS in a Coplin jar, slides were incubated with secondary antibody diluted in 3% BSA, 1 × PBS in a humid chamber at 37 °C for 1 hour. Slides were washed in the dark 3 ×5 minutes with 1 × PBS, mounted with Vectashield containing DAPI (Vector Labs). Primary antibodies used were mouse monoclonal anti-myc antibody clone 9E10 (1/100, Abcam) and rabbit polyclonal anti-Zip1 (1/50, this laboratory). Secondary antibodies used were goat anti-mouse IgG Alexa-488 and donkey anti-rabbit IgG Alexa-594 (1/200, Molecular Probes). Images of nuclei spreads were acquired on a Zeiss Axio Observer Z1 Marianas Workstation, equipped with an ORCA-Flash 4.0 camera and DAPI, FITC and Texas red filter sets, illuminated by an X-Cite 120 PC-Q light source, with a 100×/1.4 NA oil immersion objective. Marianas Slidebook (Intelligent Imaging Innovations) software was used for acquisition. Images were analyzed in Image J. Staging of nuclei spreads was based on DAPI staining and Zip1 immunufluorescence patterns, with nuclei showing a diffuse DAPI signal with either a single bright Zip1 focus or a few small Zip1 foci counted as leptotene or zygotene cells, respectively.

Southern blot analysis of DSBs

Meiotic DSB analysis by Southern blotting was performed as described[48]. Briefly, synchronized cultures undergoing meiosis were harvested at the indicated time. After DNA purification, 800 ng of genomic DNA was digested by PstI and separated on a 1% TBE-agarose gel. DNA was transferred to Hybond-XL nylon membranes by vacuum transfer,

hybridized with *SLY1* probe (amplified with primers: 5′-GCGTCCCGCAAGGACATTAG, 5′-TTGTGGCTAATGGTTTTGCGGTG) and developed by autoradiography.

Spo11-oligo labeling

Procedure for labeling Spo11-associated oligonucleotides has been described[49]. Briefly, yeast cultures were harvested 4 hours into meiosis and denatured extracts were prepared by trichloroacetic acid precipitation. Proteins were solubilized in 2 % SDS, 500 mM Tris-HCl pH 8.1, 10 mM EDTA. Extracts were diluted in an equal volume of 2 × IP Buffer (2 % Triton X100, 30 mM Tris-HCl pH 8.1, 300 mM NaCl, 2 mM EDTA, 0.02 % SDS) and Flag-tagged Spo11-oligo complexes were immunoprecipitated on IgG-conjugated agarose beads with mouse monoclonal M2 anti-Flag antibody. DNA was labeled on the beads with terminal deoxynucleotidyl transferase and [α-^{32}P]-dCTP. After washing the beads in 1 × IP buffer, proteins were eluted with LDS sample buffer and separated by SDS-PAGE. The gel was dried and developed by autoradiography.

Western blotting of yeast meiotic extracts

Denaturing whole-cell extracts were prepared in 10% trichloroacetic acid with agitation in the presence of glass beads. Precipitated proteins were solubilized in Laemmli sample buffer and appropriate amounts of protein were separated by SDS-PAGE and analyzed by western blotting. Antibodies were mouse monoclonal anti-myc (1/2000, Abcam), rabbit polyclonal anti-Kar2 (y-115) (1/2000, Santa Cruz), HRP-conjugated mouse monoclonal anti-Flag M2 (1:2000, Sigma), mouse monoclonal anti-MBP (1:2000, NEB). Secondary antibodies were used at 1/5000: IRDye 800CW goat anti-mouse IgG, IRDye 680 goat anti-rabbit IgG. Western blots were revealed using the Li-COR Bioscience Odyssey infrared imaging system.

Yeast two hybrid

Y2H vectors were transformed separately in haploid strains SKY661 and SKY662 and selected on appropriate synthetic dropout medium. Strains were mated and streaked for single diploid colonies on medium lacking tryptophan and leucine. Single colonies were grown overnight in selective medium containing 2% glucose. Cultures were diluted in fresh medium containing 2% galactose and 1% raffinose and grown until log phase (4 hours). Cells were lysed and quantitative β-galactosidase assay was performed using ONPG substrate following standard protocols (Clontech Laboratories).

Fluorescence recovery after photobleaching (FRAP)

FRAP experiments were performed on a ZEISS LSM 880 confocal microscope at room temperature. Condensates were assembled in 15 μl reactions with 200 nM ^{Alexa488}Mer2 or 20 nM ^{Alexa594}Rec114–Mei4 mixed with 150 ng pUC19 plasmid DNA in buffer containing 25 mM Tris-HCl pH 7.5, 5% glycerol, 120 mM NaCl, 2 mM DTT, 1 mg/ml BSA, 5 mM $MgCl_2$, 5% PEG 8000, incubated at 30 °C for 30 minutes, then loaded into a 384-well glass-bottom microplate (Greiner bio-one) pre-coated with 1 mg/ml BSA (Sigma). Droplets were photobleached with 20% laser power for 1 second using 488-nm and 594-nm lasers. Time-lapse images were acquired with a 10-second interval and processed using FIJI.

Europe PMC Funders Author Manuscripts

Fluorescence intensities of regions of interest were corrected by unbleached control regions and then normalized to pre-bleached intensities.

Pulldown assay

^{HisFlag}Rec114–^{MBP}Mei4 complexes were expressed in 50 ml Sf9 cultures and purified by sequential affinity chromatography on NiNTA resin and amylose resin following a similar procedure as described above. After immobilization on amylose, one sixth (50 µl) of the resin was equilibrated in buffer containing 25 mM Hepes pH 7.5, 150 mM NaCl, 10% glycerol, 1 mM DTT, 2 mM EDTA, and 0.1% Triton. Resin without Rec114–Mei4 complexes was used as a control. The resin was incubated with 500 µl of buffer containing 5 µg of purified Mer2. After 30 min incubation on a rotating wheel at 4 °C, the resin was collected by gentle centrifugation, washed twice with 1 ml buffer, the proteins were resuspended in Laemmli buffer and analyzed by SDS-PAGE.

Partial proteolysis

For Mer2 (WT or KRRR mutant), 2 µg of protein was digested in 20 µl reactions in 100 mM Tris-HCl pH 8, 12.5 mM HEPES-NaOH pH 7.5, 150 mM NaCl, 5% glycerol, 2.5 mM EDTA, 0.5 mM DTT and the indicated amount of trypsin. For ^{HisFlag}Rec114–^{MBP}Mei4 (WT or 4KR), 1 µg of protein was digested in 30 µl reactions containing 100 mM Tris-HCl pH 8, 20 mM HEPES-NaOH pH 7.5, 240 mM NaCl, 8% glycerol, 4 mM EDTA, 0.8 mM DTT and the indicated amount of trypsin. After 30 minutes at room temperature, reactions were stopped with 0.2 mM PMSF and Laemmli buffer, and proteins were analyzed by SDS-PAGE.

Statistics and reproducibility

Micrographs shown in the article are representative images to illustrate the observations. Sample numbers in quantifications are indicated in the figure legends. Fig. 1b, g: Purified proteins were analyzed by gel electrophoresis more than three times. Fig. 2c: Condensates were imaged by AFM at least three times, typically with dozens of condensates observed for each experiment. Protein complexes without DNA were imaged at least twice in different buffers with similar results. Fig. 2d: Quantification is shown for a time course performed once, but the pattern was confirmed at least once independently. Fig. 3a: Quantification is shown for one experiment, but the DNA-binding defect of the mutant was confirmed at least twice independently using different substrates. Fig. 3b: Quantification is shown for one experiment, but the condensation defect of the mutant was confirmed at least twice independently in different conditions. Fig. 3c: Quantification is shown with data pooled from two cultures. The observation was reproduced at least twice independently. Fig. 3d: Southern blot analysis was performed with two independent cultures with identical results. Fig. 4a: Co-localization was observed more than three times in different conditions. Fig. 4b: The pattern was observed at least twice independently. Fig. 4c: Quantification is shown for a time course performed once. Fig. 4d: The observation was reproduced more than three times. Fig. 4e: Quantification is shown for a titration performed once. Fig. 4g: Quantification is shown for an experiment with four replicates. The experiment was repeated once with similar results. Fig. 4h: Southern blot is shown for a time course performed once. Fig. 4i: Quantification is shown with data pooled from two independent cultures. Extended Data Fig.

Europe PMC Funders Author Manuscripts

1b, g, i: Observations were reproduced at least once independently. Extended Data Fig. 1l: Southern blot is shown for a time course performed once. Extended Data Fig. 1g: Quantification is shown for an experiment with four replicates. The experiment was repeated once with similar results. Extended Data Fig. 1n: The experiment was performed with two independent cultures with identical results. Extended Data Fig. 2a, b: Titrations were repeated at least once with identical results. Extended Data Fig. 2c, d: Competition was performed once. Extended Data Fig. 2e, f: The observations were reproduced at least twice independently. Extended Data Fig. 2g: Condensates were imaged by AFM at least three times, typically with dozens of condensates observed for each experiment. Protein complexes without DNA were imaged at least twice in different buffers with similar results. Extended Data Fig. 4g, h: Observation reproduced at least once independently. Extended Data Fig. 6a, c: Truncation analyses were performed at least twice. Extended Data Fig. 6b, d: Quantifications are shown for one experiment, but the DNA-binding and condensation defects of the mutant was confirmed at least twice independently in different conditions. Extended Data Fig. 6g: Experiment were performed with two independent cultures with identical results. Extended Data Fig. 6h: Patterns were confirmed at least once. Extended Data Fig. 6i: Time course was performed once. Extended Data Fig. 6j: Southern blot analysis was performed with two independent cultures with identical results. Extended Data Fig. 7a: Experiment was performed once. Extended Data Fig. 7c: Experiment was performed at least twice. Extended Data Fig. 7d: Pulldown was repeated at least twice independently.

Europe PMC Funders Author Manuscripts

Extended Data

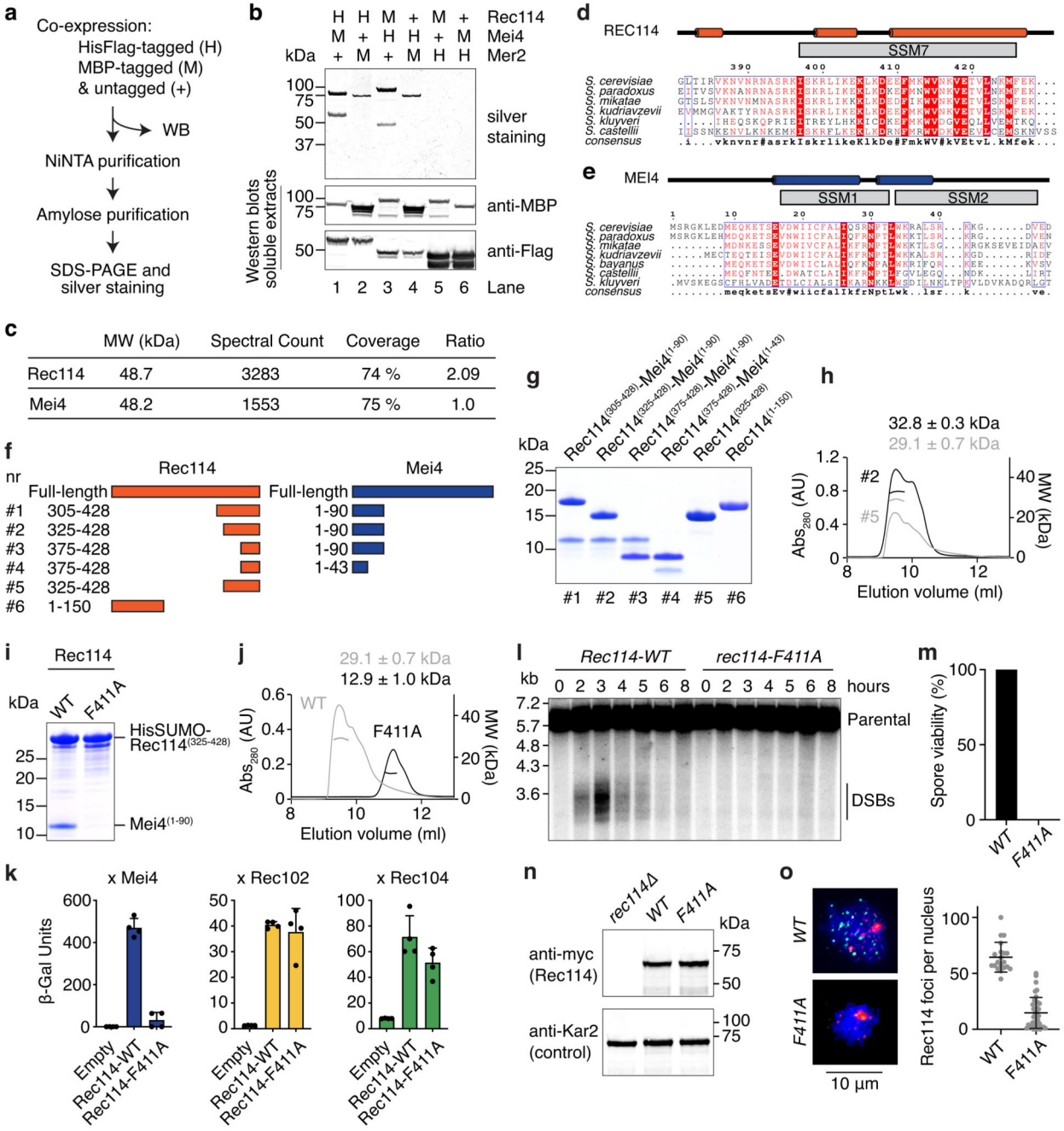

Extended Data Fig. 1. Characterization of the Rec114–Mei4 complex.

a. Strategy for purification of a hypothetical Rec114–Mei4–Mer2 (RMM) complex. Combinations of MBP-tagged and HisFlag-tagged RMM subunits were co-expressed in insect cells. After cell lysis, complexes were purified by sequential affinity chromatography and analyzed by SDS-PAGE. Expression and solubility of the recombinant proteins are verified by western blotting (WB) of cell extracts. **b**. Analysis of purified complexes.

Rec114–Mei4 complexes were apparent (lanes 1 and 3), but no Mer2 was co-purified. Lanes 2 and 4 show some enrichment of MBP-Mer2, but no co-purification of Rec114–Mei4. The presence of MBP-Mer2 in lanes 2 and 4 of the silver-stained gel may be due to background binding of MBP-Mer2 to the NiNTA resin (potentially via adsorption of DNA to the resin), or to low-affinity interactions to immobilized His-tagged Rec114–Mei4 complexes. Either way, none of the combinations tested yielded stoichiometric complexes of all three RMM subunits. Western blot controls of cell extracts showed that the tagged RMM proteins were expressed and soluble. **c**. Mass spectrometry analysis of Rec114–Mei4 complexes. Purified Rec114-Mei4 complexes were treated with trypsin and analyzed by LC-MS/MS. The ratio of spectral counts between Rec114 and Mei4 provides additional evidence supporting the 2:1 stoichiometry of the complex. **d**, **e**. Alignments and predicted secondary structures of the C-terminus of Rec114 (**d**) and the N-terminus of Mei4 (**e**). The positions of the conserved SSMs are indicated. **f**. Cartoon of the Rec114–Mei4 truncations analyzed. **g**. Purification of Rec114–Mei4 truncations. Proteins were expressed in *E. coli* and purified on NiNTA resin using a HisSUMO tag fused to the N-terminus of the Rec114 fragment. After removal of the tag by treatment with the SUMO protease Ulp1, complexes were further purified by gel filtration. A Coomassie-stained SDS-PAGE analysis of purified complexes is shown. 5 μg was loaded for each sample. Polypeptides containing $Rec114^{(375-428)}$ and $Mei4^{(1-43)}$ retained the ability to interact (combination #4). **h**. SEC-MALS analysis of Rec114–Mei4 truncations. The data are consistent with expectation for truncations that contain two Rec114 subunits and one Mei4 subunit. The C-terminus of Rec114 alone forms a dimer. **i**. Wild type and F411A-containing variants of $^{HisSUMO}Rec114^{(325-428)}$ were co-expressed with $Mei4^{(1-90)}$ and purified by chromatography on NiNTA resin. The absence of the Mei4 fragment with Rec114-F411A shows that the mutation abolishes the interaction with Mei4. **j**. SEC-MALS analysis of untagged wild-type (WT, reproduced from panel H to aid comparison) and F411A $Rec114^{(325-428)}$ show that the mutation affects Rec114 dimerization. **k**. Y2H analysis of the interaction of Gal4BD-Rec114 (WT and F411A) with LexA-Mei4, LexA-Rec102, or LexA-Rec104 (mean and SD from four replicates). β-Gal units are quantified based on hydrolysis of ONPG. The F411A mutation abolishes the interaction of Rec114 with Mei4, but not with Rec102 and Rec104. **l**. Southern blot analysis of meiotic DSB formation at the *CCT6* hotspot, showing that *rec114-F411A* is defective in meiotic DSB formation. **m**. Spore viability of *rec114-F411A* mutant (n = 40). **n**. Western-blot analyses of meiotic protein extracts from myc-tagged *REC114-WT* and *F411A* strains. The F411A mutation does not compromise the expression of Rec114. **o**. Immunofluorescence microscopy analysis of meiotic chromosome spreads with wild-type and F411A myc-tagged Rec114. Green, anti-myc; red, synaptonemal complex component Zip1; blue, DNA. Quantification of the number of Rec114 foci per leptotene or early zygotene cell is plotted; error bars show mean ± SD (n = 20 and 38 cells for WT and F411A, respectively). The F411A mutation abolishes the formation of chromatin-associated Rec114 foci.

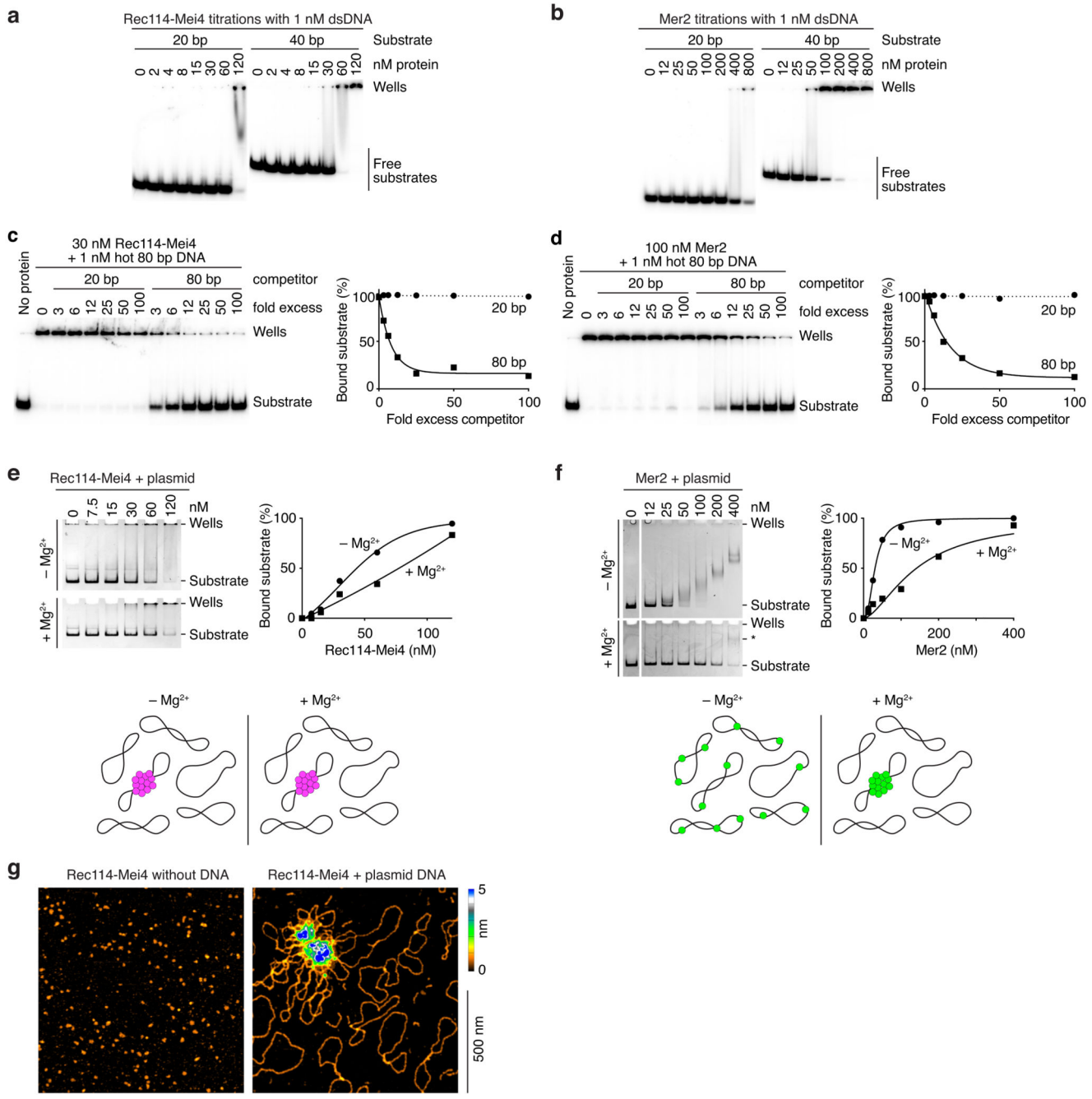

Extended Data Fig. 2. DNA-binding properties of Rec114–Mei4 and Mer2 complexes.

a, **b**. Gel shift analysis of Rec114–Mei4 (**a**) or Mer2 (**b**) binding to 20- or 40- bp DNA substrates. Quantification is in Fig. 2b. **c**, **d**. Competition assay of Rec114–Mei4 (**c**) or Mer2 (**d**) binding to 80 bp radiolabeled DNA (1 nM) in the presence of 20- or 80 bp cold competitor. Fold excess is in nucleotides. Lines are one-phase decay fits. **e**, **f**. Binding to plasmid DNA analyzed by native agarose gel electrophoresis. Rec114–Mei4 (**e**) and Mer2 (**f**) were titrated with 2 nM plasmid DNA (pUC19) in the presence or absence of 5 mM $MgCl_2$. Rec114–Mei4 complexes bound with roughly similar affinity independently of the

Europe PMC Funders Author Manuscripts

Europe PMC Funders Author Manuscripts

presence of Mg^{2+} (apparent $K_D \approx 50–80$ nM). Note that the apparent affinity is significantly lower than suggested by the gel shift analyses with radiolabeled substrates presented in panel **a** and Fig. 2a, b (see apparent affinities in Fig. 2 legend). We interpret that this difference is because the proteins coalesce on a small fraction of the plasmid molecules, as illustrated in the cartoon below. Indeed, bound plasmids remained trapped in the wells, which is consistent with cooperative assembly of large nucleoprotein structures. Because each plasmid substrate provides many more binding sites than the short oligonucleotide substrates in panel **a** and Fig. 2a, a higher concentration of protein is required to reach complete binding of all of the plasmid molecules. In contrast to Rec114–Mei4, Mer2 showed efficient binding in the absence of Mg^{2+} in this assay ($K_D = 30 \pm 2$ nM) but binding appeared to be considerably inhibited in the presence of Mg^{2+} ($K_D \approx 150$ nM), as indicated by the persistence of unbound substrate at high protein concentrations. However, while the electrophoretic mobility of Mer2-bound plasmids decreased steadily as the concentration of Mer2 increased in the absence of Mg^{2+}, no such steady progression was observed when Mg^{2+} was included. Instead, a minority of bound substrates shifted to a low-mobility species (labeled * in panel **f**, bottom), indicating that they were occupied by multiple Mer2 complexes. We interpret that, rather than inhibiting DNA binding, Mg^{2+} promotes cooperativity, in agreement with the fluorescence microscopy analysis (Extended Data Fig. 3b). The difference in migration distance of the plasmid between the +/- Mg^{2+} gels is due to the presence of Mg^{2+} in the electrophoresis buffer. **g**. AFM imaging of 12 nM Rec114–Mei4 in the absence (left) or in the presence (right) of 1 nM plasmid DNA (pUC19).

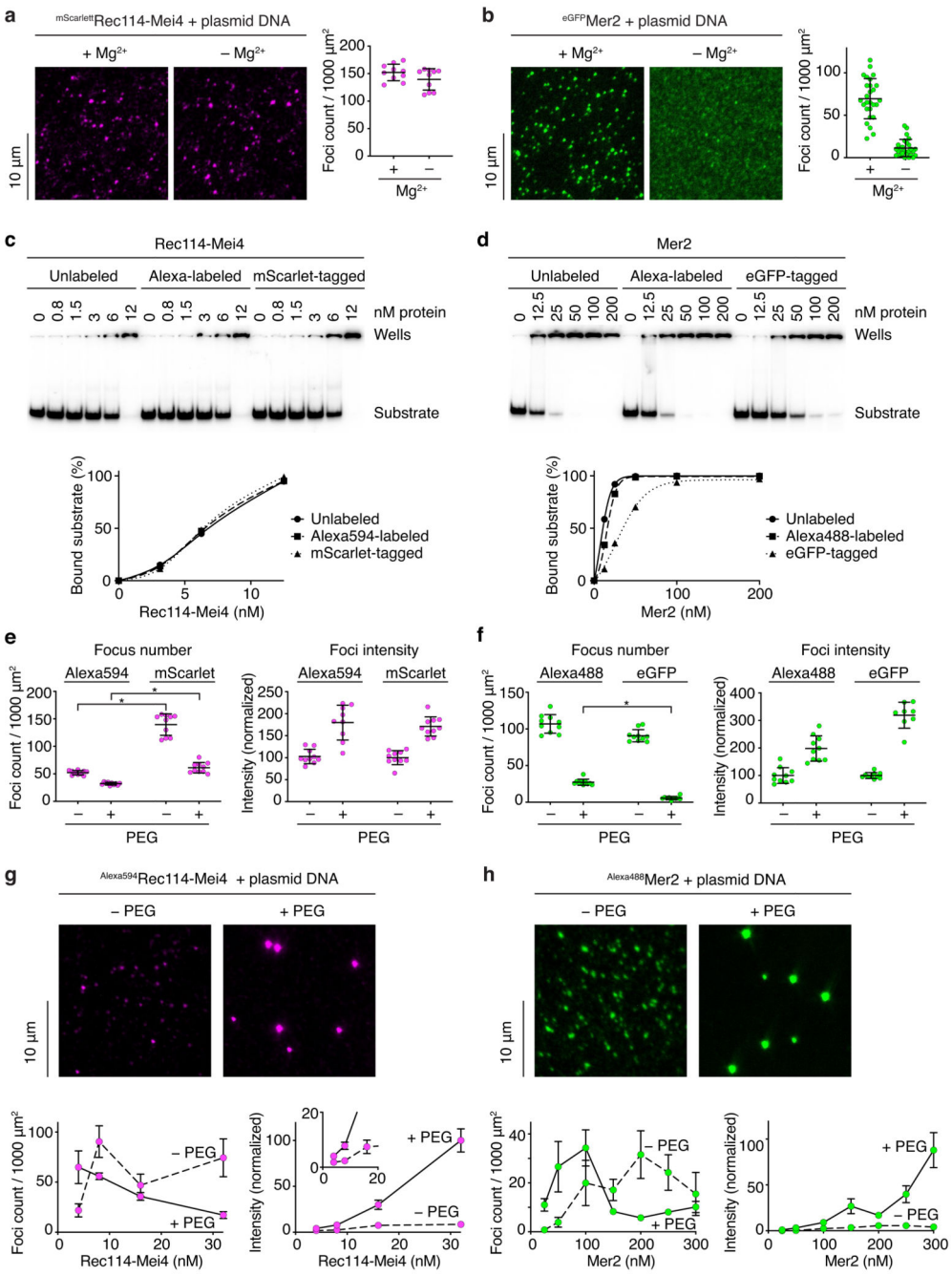

Extended Data Fig. 3. Properties of Rec114–Mei4 and Mer2 DNA-dependent condensates.

a, **b**. Visualization of nucleoprotein condensates by epifluorescence microscopy using tagged Rec114–Mei4 (**a**) or Mer2 (**b**) in the presence or absence of 5 mM $MgCl_2$. Foci were defined using a fixed intensity threshold between samples. Each point represents the measurement from a field of view. Error bars show mean ± SD from (a) 10 fields of view of 1.7×10^4 µm^2 or (b) 27 and 26 sections of 400 µm^2 with and without Mg^{2+}, respectively. **c**-**f**. Effect of fluorophore labeling or tagging on the DNA-binding and DNA-driven condensation activities of Rec114–Mei4 and Mer2 complexes. Labeling with Alexa594 or

Europe PMC Funders Author Manuscripts

Alexa488 was achieved using amine-reactive fluorophores. Tagging was achieved by fusion of Rec114 with the monomeric fluorescent protein mScarlet or fusion of Mer2 with the weakly dimerizing fluorescent protein eGFP. The results described here indicate that the covalent Alexa labeling has little if any effect on DNA binding properties of these complexes, whereas fluorescent protein tagging caused subtle alterations in DNA binding and/or condensation. In most subsequent experiments, we used the dye-labeled complexes to minimize steric effects or oligomerization of fluorescent protein tags. **c**. Gel-shift analysis of binding of unlabeled, Alexa594-labeled, or mScarlet-tagged Rec114–Mei4 complexes to an 80-bp radiolabeled DNA substrate. The three versions of the Rec114–Mei4 complex have the same intrinsic DNA-binding activity. **d**. Gel-shift analysis of binding of unlabeled, Alexa488-labeled, or eGFP-tagged Mer2 complexes to an 80-bp radiolabeled DNA substrate. The DNA-binding activity of the Alexa-labeled Mer2 complex is nearly identical to the untagged protein, but the eGFP-tagged complex has 3.5-fold reduced DNA-binding activity. **e**. A comparison between Alexa-labeled and mScarlet-tagged Rec114–Mei4 complexes for DNA-driven condensation. Focus numbers (left graphs) and total fluorescence intensity within foci normalized to the no-PEG samples (right graphs) are shown for the complexes in the presence or absence of 5% PEG. With and without PEG, mScarlet-tagged Rec114–Mei4 produced more foci than the Alexa-labeled version. Because intrinsic DNA binding was indistinguishable between the complexes (panel **c**), we infer that the mScarlet-tagged complexes had a reduced efficiency in the cooperative formation of large condensates compared to the Alexa-labeled version, producing more numerous foci. Asterisk indicates $p < 0.0001$ (two-tailed t test). Lines and error bars are mean ± SD from 8–10 fields of view. **f**. A comparison between Alexa-labeled and eGFP-tagged Mer2 complexes for DNA-driven condensation. Quantification is presented as in panel **e**. The two labeled complexes show different numbers and intensities of foci in the presence of PEG. It is likely that the DNA-binding defect of the eGFP construct (panel **d**) leads to the formation of fewer, brighter condensates. It is possible that the weak dimerization activity of eGFP also contributes. Asterisk indicates $p < 0.0001$ (two-tailed t test). Lines and error bars are mean ± SD from 9–10 fields of view. **g**, **h**. Effect of a crowding agent (PEG) on formation of nucleoprotein condensates visualized using covalently fluorophore-labeled Rec114–Mei4 (**g**) or Mer2 (**h**). Graphs show the effect of protein concentration on DNA-driven condensation in the presence or absence of 5% PEG. Left graphs show focus numbers and right graphs show the total fluorescence intensity within foci (normalized to the mean of the highest intensity sample). Points and error bars are means ± SD from 4–6 fields of view (**g**) or 7–10 fields of view (**h**). The titrations reveal complex behaviors: (**g**) In the presence of PEG, titration of Rec114–Mei4 from 4 to 32 nM led to a steady decrease in the number of foci, which was accompanied by a concomitant increase in focus intensity. In the absence of PEG, however, the number of Rec114–Mei4 foci first peaked at 8 nM before decreasing as the intensity of the foci started to increase. Nevertheless, focus intensity plateaued at a much lower intensity than in the presence of PEG. (**h**) In the case of Mer2, titration from 25 to 300 nM in the presence of PEG yielded a peak in the number of foci at ~100 nM, which then sharply declined and stabilized beyond 150 nM. Consistently, Mer2 foci remained at a constant, low intensity between 25 and 100 nM, then became abruptly brighter above 100 nM. In the absence of PEG, the number of Mer2 foci increased between 25 and 200 nM, then started to decrease beyond that threshold. These behaviors likely reflect complex combined effects of

nucleation, growth, and collapse of the condensates, which are each affected differently by protein concentrations and by the crowding effect provided by PEG. See Source Data for exact n values for panels e, f, g, and h.

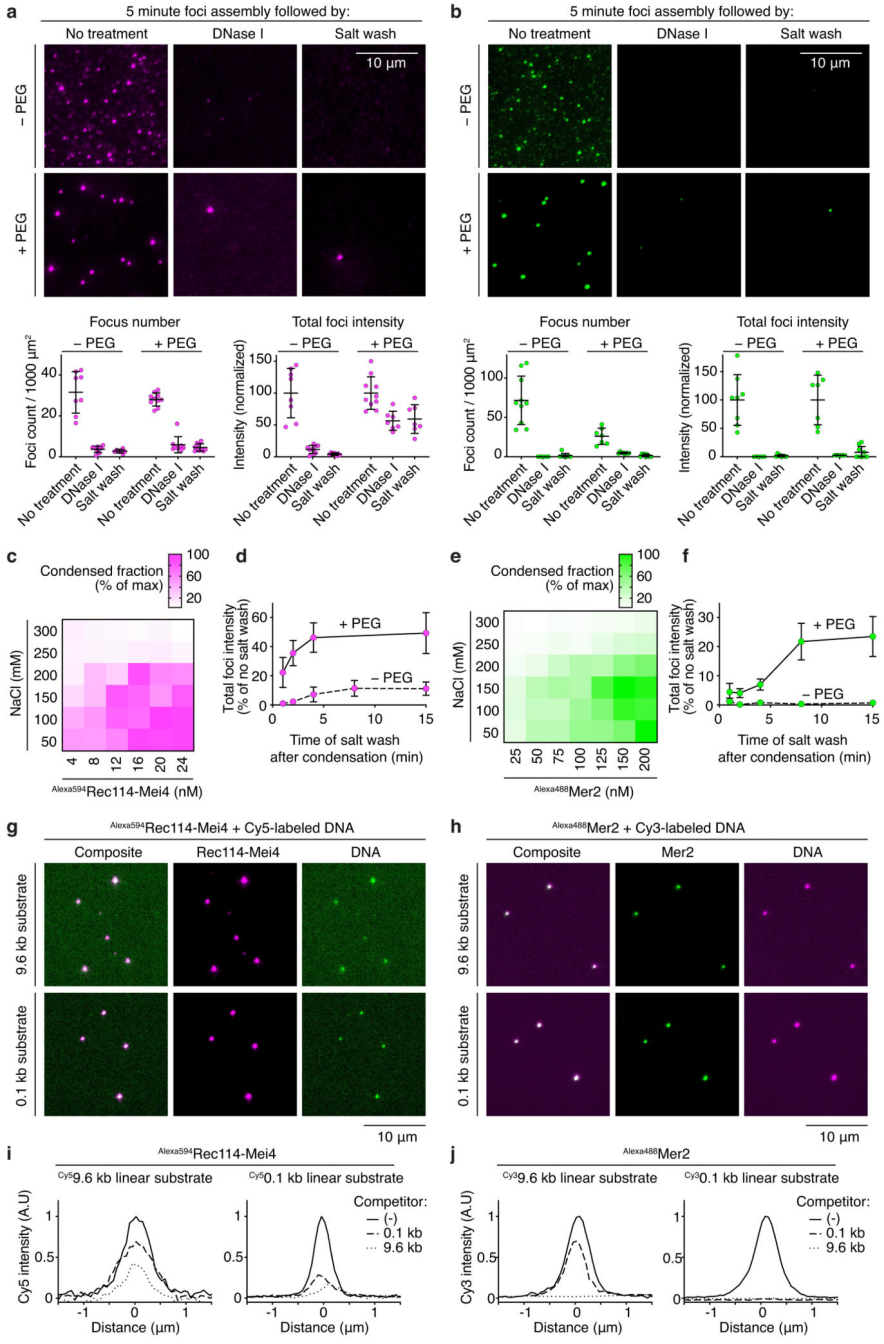

Extended Data Fig. 4. Properties of Rec114–Mei4 and Mer2 DNA-dependent condensates.

a, b. Effect of challenging Rec114–Mei4 (**a**) or Mer2 (**b**) nucleoprotein condensates with DNase I or 0.5 M NaCl. Condensates were assembled for 5 minutes prior to challenge. Quantification is provided of focus numbers per 1000 µm^2 and of the total fluorescence

Europe PMC Funders Author Manuscripts

intensity within foci within fields of view (normalized to mean of the no-treatment controls). Error bars show mean ± SD from 5–10 fields of view. **c, e**. Titrations of Rec114–Mei4 (**c**) and Mer2 (**e**) in the presence of DNA and PEG and various concentrations of NaCl. Heat maps represent the fraction of fluorescence signal found within foci. Condensed fractions are maximal at high protein and low salt concentrations. At all protein concentrations, condensation is essentially abolished beyond 250 mM NaCl. This suggests that electrostatic interactions, likely between the negatively charged DNA backbone and positively charged protein residues, are important for condensation. **d, f**. Time dependence for irreversibility of Rec114–Mei4 (**d**) and Mer2 (**f**) condensates. Some phase-separated liquid droplets have been shown to mature over time and progressively adopt gel-like or solid states[35,37–39]. Such sol-gel transitions may occur spontaneously through different mechanisms, including fibrillization and entanglement, and are thought to be counteracted *in vivo* to prevent the progressive accumulation of amyloid-like structures associated with pathological states[35]. To address whether our condensates are prone to progressive hardening, we queried the effect of assembly time on reversibility. We performed a time-course experiment where the condensates were challenged by treatment with 0.5 M NaCl after an indicated period of assembly in the presence or absence of PEG. The graph shows the total intensity summed for foci within fields of view, expressed as a percentage of the intensity without a salt challenge. Points and error bars are means ± SD for 6–10 fields of view. With Rec114–Mei4, 10% and 50% of fluorescent signal became refractory to the salt wash within 5 minutes of incubation time in the absence and presence of PEG, respectively (see panel **a** for example images and quantification). With Mer2, there was no evidence for the formation of irreversible structures in the absence of PEG during the course of the experiment. However, up to 25% of the focus intensity resisted the salt wash treatment after 8 minutes of incubation time in the presence of PEG. Therefore, both Rec114–Mei4 and Mer2 have a propensity to form more stable, perhaps gel-like, structures over time. Under our experimental conditions, this was more evident for Rec114–Mei4 than for Mer2, and was accentuated by molecular crowding. **g, h**. Assembly of Rec114–Mei4 (**g**) and Mer2 (**h**) with fluorescently labeled 9.6 kb and 100 bp linear DNA substrates. The overlap between the protein foci and puncta of DNA shows that the DNA is also enriched in the condensates. However, in contrast to the protein signal, the fluorescent signal of the DNA covers the slide because DNA is in excess and does not condense by itself. **i, j**. Competition between long and short DNA substrates for incorporation into condensates. Rec114–Mei4 (**i**) or Mer2 (**j**) condensates were assembled in the presence of a fluorescently labeled DNA substrate with or without 20-fold nucleotide excess of unlabeled competitor. The amount of fluorescent DNA signal averaged between ten foci is plotted. In each case, the 9.6-kb substrate was a more effective competitor than the 100-bp substrate. In addition, the 100-bp substrate was more successful at competing with the 100-bp fluorescent substrate than with the 9.6-kb fluorescent substrate. This preference for large DNA substrates is consistent with the hypothesis that the condensates form through multivalent interactions between the positively charged residues of Rec114-Mei4 or Mer2 and the sugar-phosphate backbone of the DNA. See Source Data for exact n values for panels a, b, d, and f.

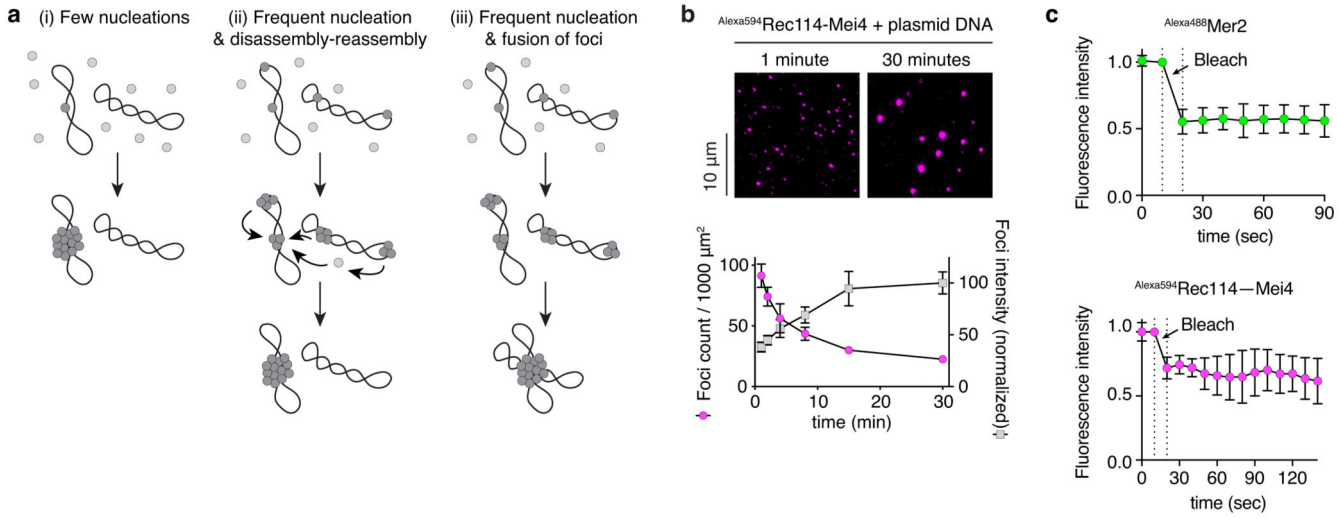

Extended Data Fig. 5. Growth of DNA-driven condensates by fusion.

a. Three scenarios for the assembly of DNA-driven condensates. (i) Nucleation could be limiting, with focus growth resulting principally from incorporation of protein from soluble pools. (ii) Frequent nucleation events could occur initially leading to large numbers of small foci, whereupon some foci dissolve and others grow. (iii) Frequent nucleation could yield numerous small foci that then collide and fuse to yield fewer, larger foci. See Supplementary Discussion 2 for more detail. **b**. Time course of the assembly of Rec114–Mei4 foci in the presence of plasmid DNA. The x axis indicates the time in solution before plating, upon which DNA is immobilized to the glass slide while soluble protein is still free to diffuse. Quantification is provided of focus numbers and average focus intensity (normalized to the mean at 30 min). Error bars show mean ± SD from 10 fields of view. **c**. FRAP experiments with Mer2 and Rec114–Mei4 condensates. Points and error bars are mean ± SD for six photobleached condensates.

Europe PMC Funders Author Manuscripts

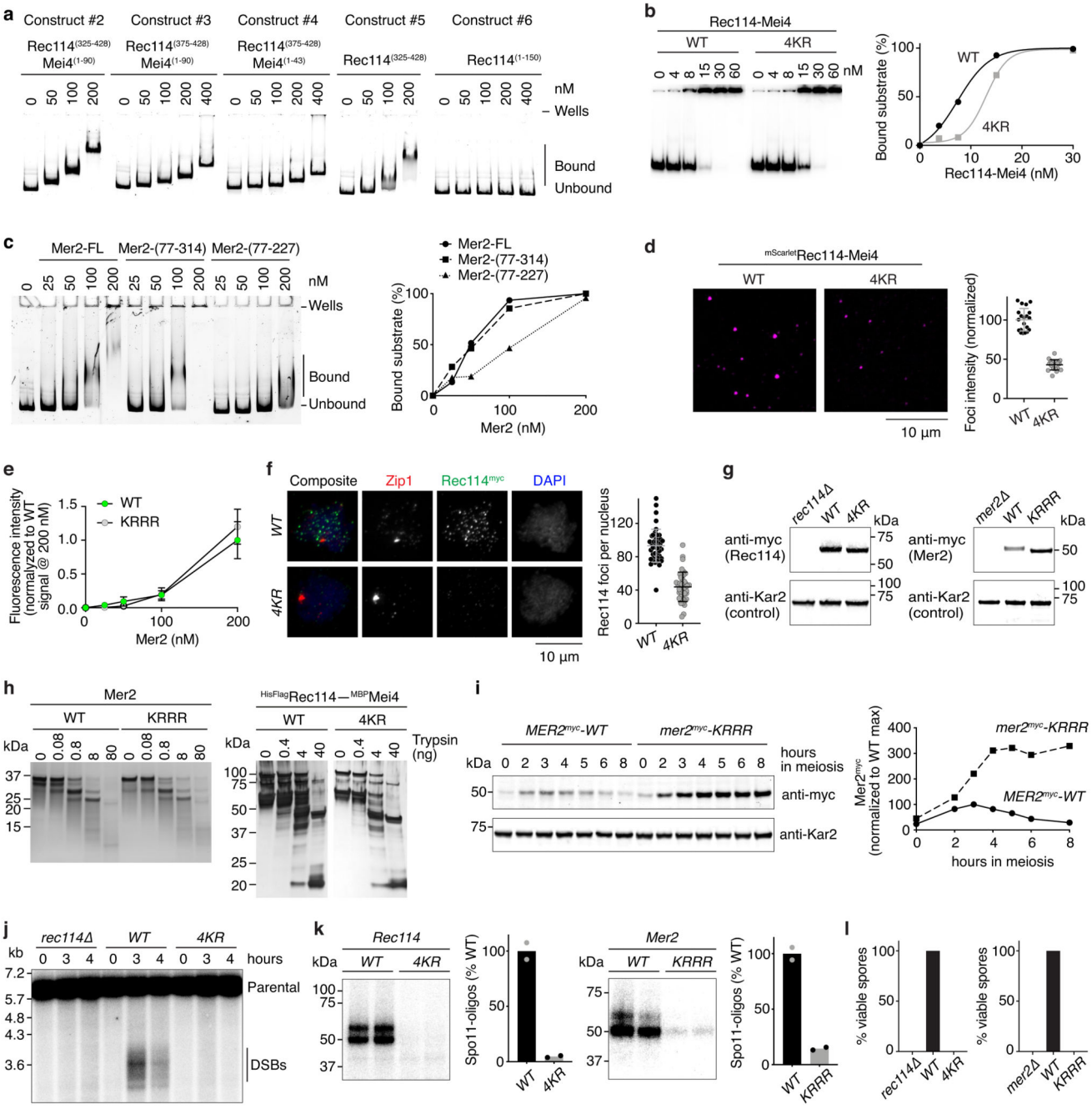

Extended Data Fig. 6. Identification of DNA-binding residues and effect of DNA binding on condensation *in vitro* and *in vivo* and on Spo11-induced break formation.

a. Mapping the DNA-binding domain of Rec114–Mei4 complexes. Gel-shift analysis was performed with pUC19 plasmid DNA and the Rec114–Mei4 protein constructs shown in Extended Data Fig. 1f. Constructs #2, #3 and #4, which include the C terminus of Rec114 and the N terminus of Mei4, were competent for DNA binding. The difference in mobility of shifted species between these constructs is in line with the difference in sizes of the protein complexes. Mei4 is dispensable for DNA binding by Rec114 (Construct #5 lacks Mei4). The

Europe PMC Funders Author Manuscripts

N terminus of Rec114 alone, encompassing the PH domain, did not bind DNA (Construct #6). None of the constructs showed evidence for cooperative DNA binding (unlike the full-length protein, see Extended Data Fig. 2e), suggesting that they do not undergo DNA-driven condensation. **b**. Gel shift analysis wild-type (WT) and mutant Rec114–Mei4 complexes binding to an 80-bp DNA substrate. The Rec114-4KR mutant has residues R395, K396, K399, and R400 mutated to alanine. Lines on graphs are sigmoidal curve fits. **c**. Mapping the DNA-binding domain of Mer2. Gel-shift analysis was performed with pUC19 plasmid DNA and HisSUMO-tagged Mer2 protein that was either full-length (FL), had the N terminus removed (fragment 77-314), or had both the N and C termini removed (fragment 77-227). Deleting the N terminus alone had no significant effect on DNA binding, but further deleting the C terminus strongly reduced DNA binding. **d**. Effect of the Rec114-4KR mutation on condensation *in vitro*. Reactions included 5% PEG. Each point is the average of the intensities of foci in a field of view (n = 20 fields), normalized to the overall mean for wild type. Error bars show mean ± SD. **e**. Incorporation of Mer2-KRRR into preformed condensates. Condensates were assembled with 100 nM unlabeled Mer2. Reactions were then supplemented with the indicated amount eGFP-Mer2 (WT or KRRR) and plated immediately. Incorporation of eGFP-tagged complexes within condensates was quantified. Points and error bars are mean ± SD from 20 fields of view. **f**. Immunofluorescence on meiotic chromosome spreads for myc-tagged Rec114. The number of foci per leptotene or early zygotene cell is plotted. Error bars show mean ± SD (n = 44 and 40 cells for *WT* and *4KR*, respectively). **g**. Immunoblotting of meiotic protein extracts for wild type and mutant Rec114 (left) or Mer2 (right). **h**. Partial proteolysis of wild-type and mutant Mer2 and Rec114–Mei4 complexes. **i**. Immunoblot analysis of Mer2-WT and Mer2-KRRR. Protein extracts of meiotic time courses were analyzed by SDS-PAGE followed by immunoblotting against Mer2-myc. Anti-Kar2 was used as a loading control. Quantification of immunoblot signal is plotted. $Mer2^{myc}$-KRRR reached higher steady-state protein levels and persisted longer than wild-type $Mer2^{myc}$. A previous study showed that mutating an essential CDK phosphorylation site of Mer2 (Ser30) or inhibiting CDK activity led to reduced turnover of Mer2, similar to the effect of the KRRR mutant[15]. This is consistent with the hypothesis that Mer2 turnover is tied to phosphorylation, which requires DNA binding. **j**. Southern blot analysis of meiotic DSB formation at the *CCT6* hotspot in strains expressing wild-type or mutant Rec114 protein. **k**. Labeling of Spo11-oligo complexes in wild type and mutant Rec114 (top) and Mer2 (bottom) strains. Error bars represent the range from two biological replicates. **l**. Spore viability of wild type and mutant Rec114 (left) and Mer2 (right) strains (n = 40). For gel source data, see Supplementary Figure 1.

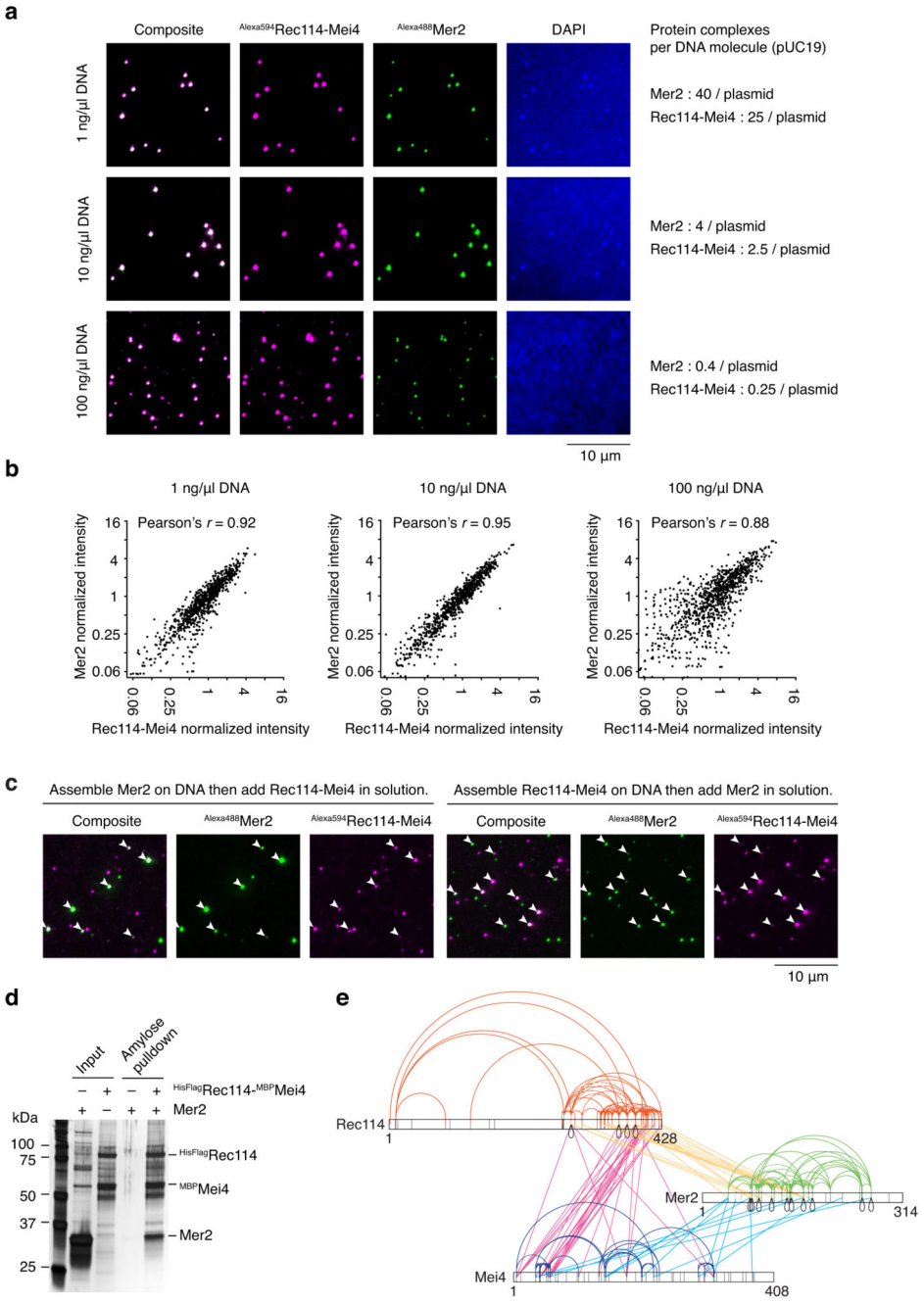

Extended Data Fig. 7. Rec114–Mei4 and Mer2 form mixed condensates.

a. Rec114–Mei4 colocalizes with Mer2 in mixed condensates irrespective of DNA concentration. Reactions containing 16 nM Rec114–Mei4 and 100 nM Mer2 in the presence of 1, 10, or 100 ng/µl plasmid DNA were assembled for 20 minutes at 30 °C. DAPI (5 µg/ml) was added to the reaction before applying to glass slides. DNA enrichment within the condensates is visible at lower DNA concentrations (top and middle rows), but is not as clear at high DNA concentrations (bottom row). The ratios of Rec114–Mei4 (heterotrimers) and Mer2 (tetramers) to each 2.6-kb plasmid DNA molecule are indicated on the right.

Europe PMC Funders Author Manuscripts

Colocalization of Rec114–Mei4 and Mer2 complexes is evident even with a molar excess of DNA molecules, demonstrating that formation of joint foci is not simply because both protein complexes are independently associating with a limiting number of DNA substrates. **b**. Correlated intensity of Rec114–Mei4 and Mer2 proteins within the condensates. Each point shows the fluorescence intensity in an individual focus (n = 950, 925 and 1000 foci from 2-3 fields of view for samples with 1, 10 and 100 ng/μl DNA, respectively), normalized to the average foci intensity per field of view. The strong correlation indicates that the composition of the condensates is highly uniform between foci. In the presence of high DNA concentration, the fraction of smaller foci increased and correlated intensities decreased. **c**. Recruitment of soluble Rec114–Mei4 (left) or Mer2 (right) into preassembled condensates of Mer2 (left) or Rec114–Mei4 (right). White arrowheads point to examples of the preassembled condensates. **d**. Pulldown of purified Mer2 on amylose resin with or without immobilized Rec114–Mei4 complexes. **e**. XL-MS of Rec114–Mei4–Mer2 condensates (620 crosslinked peptides, 229 distinct crosslinked pairs of lysines).

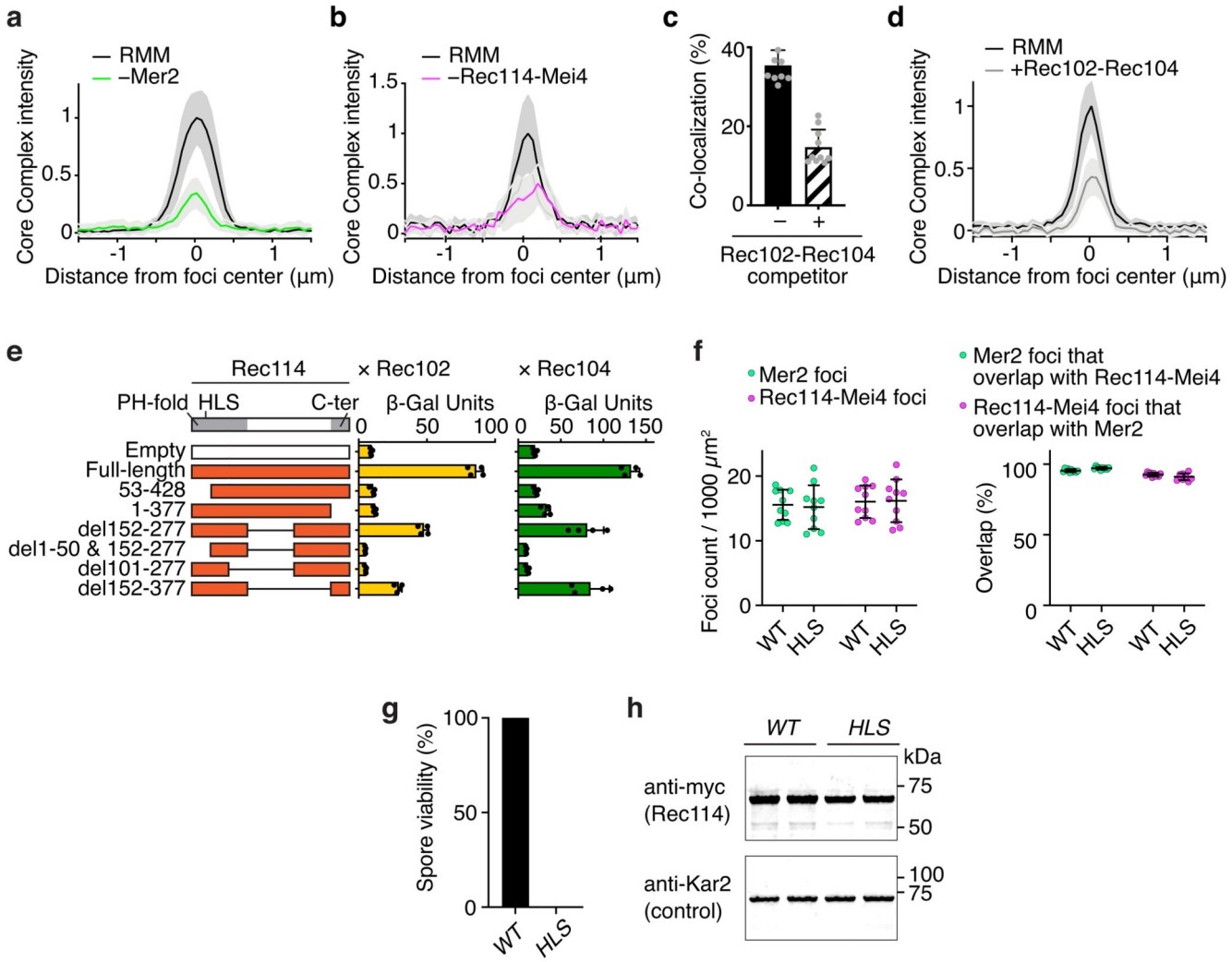

Europe PMC Funders Author Manuscripts

Europe PMC Funders Author Manuscripts

Extended Data Fig. 8. Recruitment of the Spo11 core complex to Rec114–Mei4–Mer2 condensates.

a. Quantification of core complex signal within Rec114–Mei4 foci in the presence (100 nM) or absence of Mer2. The average intensity within 20 foci is plotted for each reaction. Shaded areas represent 95% confidence intervals. **b**. Quantification of core complex signal within Mer2 foci in the presence (16 nM) or absence of Rec114–Mei4. Reactions contained 25 nM Mer2. The average intensity within 20 foci is plotted for each reaction. Shaded areas represent 95% confidence intervals. **c**. Effect of including 100 nM ^{MBP}Rec102–Rec104^{HisFlag} competitor on the recruitment of the core complex to RMM condensates (16 nM Rec114–Mei4, 100 nM Mer2). The fraction of Rec114–Mei4–Mer2 foci that contain detectable core complex signal is plotted (mean and SD from 10 fields of view). **d**. Intensity of core complex signal within Rec114–Mei4–Mer2 condensates in the absence or presence of Rec102–Rec104 competitor. The average core complex intensity within 20 foci is plotted for each reaction. Shaded areas represent 95% confidence intervals. **e**. Mapping regions of Rec114 required for interaction with Rec102 or Rec104 by Y2H analysis. ±-galactosidase units are measured for the interaction between truncated variants of Gal4AD-Rec114 and LexA-Rec102 or LexA-Rec104 (mean and SD from four replicates). The position of the HLS mutation within the Rec114 PH-fold is indicated. **f**. Impact of the HLS mutation on the formation of comingled RMM condensates. Error bars show mean ± SD from 10 fields of view. **g**. Spore viability of Rec114-WT and HLS mutant strains. **h**. Immunoblot analysis of meiotic protein extracts from myc-tagged Rec114-WT and HLS mutant strains. Samples from two biological replicates are shown. For gel source data, see Supplementary Figure 1.

Europe PMC Funders Author Manuscripts

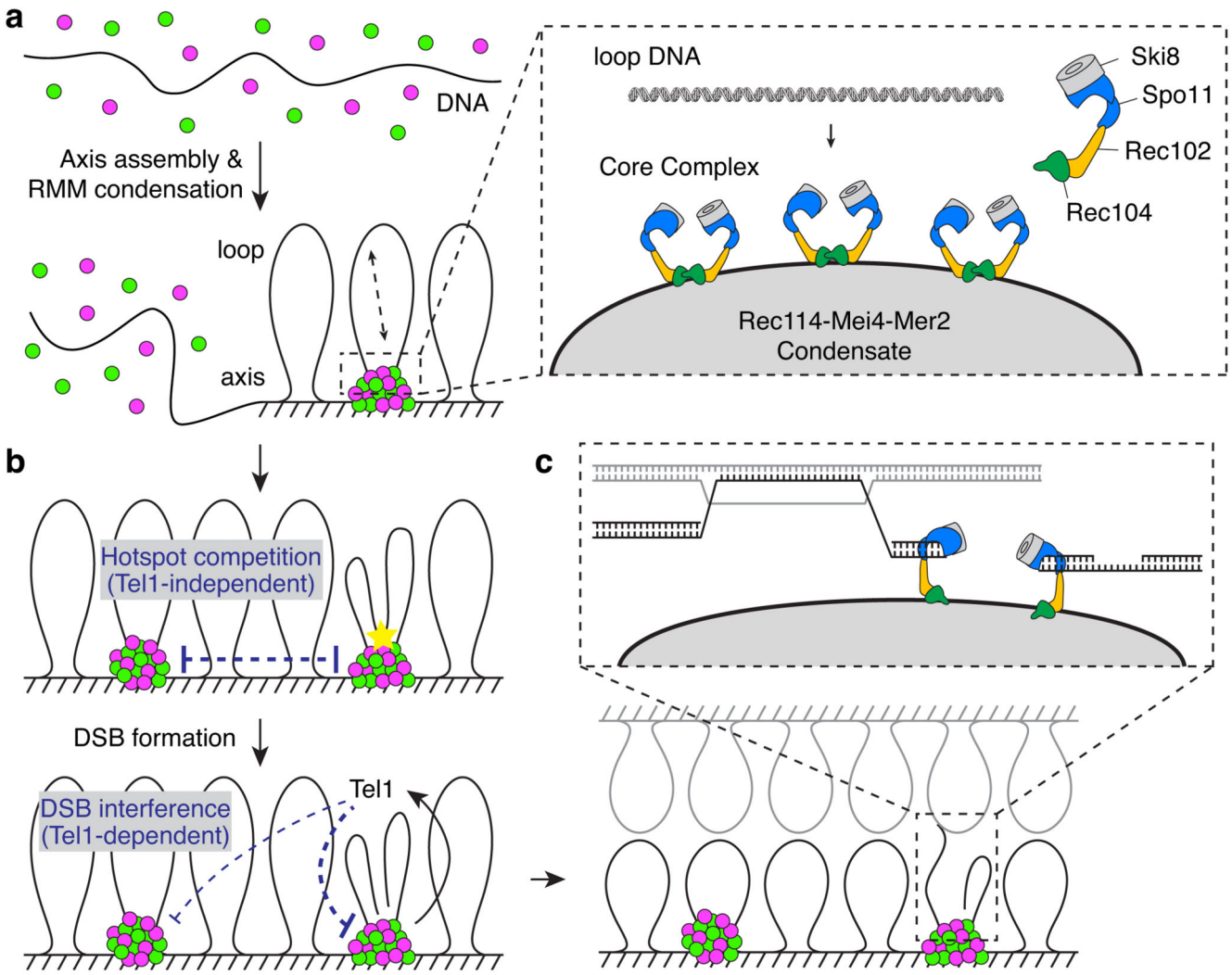

Extended Data Fig. 9. A condensate model for assembly of the meiotic DSB machinery and implications for the control of DSB formation and repair.

a. Assembly of the DSB machinery. (Left) Rec114–Mei4 and Mer2 complexes bind DNA in a highly cooperative manner to form large mixed nucleoprotein condensates. (Right) These condensates provide a platform to recruit the core complex through interactions that involve the N-terminal domain of Rec114 and the Rec102–Rec104 components of the core complex. Multiple Spo11 complexes are recruited and may engage an incoming DNA loop simultaneously. The molecular arrangement of the core complex proteins is based on ref [10]. See Supplementary Discussion 4 for more detail. **b**. Hotspot competition and DSB interference. Competition arises prior to DSB formation as a consequence of the partitioning of RMM proteins into condensates. DSB interference is implemented through local inhibition of further DSB formation by DSB-activated Tel1. Inhibition could work on the same cluster that generated the activation DSB as well as on nearby clusters in cis. See Supplementary Discussion 5 for more detail. **c**. The coherence provided by the condensates may serve functions during repair, including the maintenance of a physical connection

between the DNA ends that involves end-capping by condensate-embedded core complexes. See Supplementary Discussion 6 for more detail.

Supplementary Material

Refer to Web version on PubMed Central for supplementary material.

Acknowledgements

We thank Alain Nicolas and Valérie Borde for sharing unpublished information, Jiaqi Xu for assistance with preliminary analyses of the Mer2-KRRR mutant, and other members of the Keeney lab for discussions. We thank MSK core facilities, supported by NIH cancer center core grant P30 CA008748: Microchemistry and Proteomics (Ronald Hendrickson and Elizabeth Chang) for the XL-MS experiments, Molecular Cytology (Matthew Brendel and Yevgeniy Romin) for AFM experiments, and Sho Fujisawa for writing a Fiji script to quantify fluorescent foci. We thank Ewa Folta-Stogniew from the Biophysics Resource of Keck Facility at Yale University for the SEC-MALS experiments. The SEC-LS/UV/RI instrumentation was supported by NIH grant S10 RR023748. This work was supported by the Howard Hughes Medical Institute (SK), the Maloris Foundation (DP), an MSK Basic Research Innovation Award (SK and DP), the European Research Council under the European Union's Horizon 2020 research and innovation program (ERC grant agreement 802525 to CCB), and the Fonds National de la Recherche Scientifique (MIS-Ulysse grant F.6002.20 to CCB).

Data availability

Source data for gels, blots, and graphs for Figs. 1, 2, 3, and 4; blots for Extended Data Figs. 6 and 8; and source data for graphs in Extended Data Figs. 3, 4, 5, and 6 are available with the paper. Processed crosslinking-mass spectrometry data are provided in Supplementary Table 1. Fasta sequences of the yeast SK1 strain are available at https://www.yeastgenome.org. Swissprot reviewed database is available at www.UniProt.org.

Code availability

The custom Image J scripts for analysis of condensate foci are available at https://github.com/claeysbouuaert/scripts.

References

1. de Massy B. Initiation of meiotic recombination: how and where? Conservation and specificities among eukaryotes. Annu Rev Genet. 2013; 47:563–599. [PubMed: 24050176]
2. Lam I, Keeney S. Mechanism and regulation of meiotic recombination initiation. Cold Spring Harb Perspect Biol. 2015; 7
3. Cooper TJ, Garcia V, Neale MJ. Meiotic DSB patterning: A multifaceted process. Cell Cycle. 2016; 15:13–21. [PubMed: 26730703]
4. Keeney S, Lange J, Mohibullah N. Self-organization of meiotic recombination initiation: general principles and molecular pathways. Annu Rev Genet. 2014; 48:187–214. [PubMed: 25421598]
5. Kleckner N. Chiasma formation: chromatin/axis interplay and the role(s) of the synaptonemal complex. Chromosoma. 2006; 115:175–194. [PubMed: 16555016]
6. Keeney S, Giroux CN, Kleckner N. Meiosis-specific DNA double-strand breaks are catalyzed by Spo11, a member of a widely conserved protein family. Cell. 1997; 88:375–384. [PubMed: 9039264]
7. Bergerat A, et al. An atypical topoisomerase II from Archaea with implications for meiotic recombination. Nature. 1997; 386:414–417. [PubMed: 9121560]
8. Robert T, et al. The TopoVIB-Like protein family is required for meiotic DNA double strand break formation. Science. 2016; 352:943–949. [PubMed: 27199419]

Europe PMC Funders Author Manuscripts

9. Vrielynck N, et al. A DNA topoisomerase VI-like complex initiates meiotic recombination. Science. 2016; 352:939–943.
10. Claeys Bouuaert C, et al. Structural and functional characterization of the Spo11 core complex. Nature Structural & Molecular Biology. 2021
11. Li J, Hooker GW, Roeder GS. Saccharomyces cerevisiae Mer2, Mei4 and Rec114 form a complex required for meiotic double-strand break formation. Genetics. 2006; 173:1969–1981. [PubMed: 16783010]
12. Maleki S, Neale MJ, Arora C, Henderson KA, Keeney S. Interactions between Mei4, Rec114, and other proteins required for meiotic DNA double-strand break formation in Saccharomyces cerevisiae. Chromosoma. 2007; 116:471–486. [PubMed: 17558514]
13. Steiner S, Kohli J, Ludin K. Functional interactions among members of the meiotic initiation complex in fission yeast. Curr Genet. 2010; 56:237–249. [PubMed: 20364342]
14. Miyoshi T, et al. A central coupler for recombination initiation linking chromosome architecture to S phase checkpoint. Mol Cell. 2012; 47:722–733. [PubMed: 22841486]
15. Henderson KA, Kee K, Maleki S, Santini PA, Keeney S. Cyclin-dependent kinase directly regulates initiation of meiotic recombination. Cell. 2006; 125:1321–1332. [PubMed: 16814718]
16. Panizza S, et al. Spo11-accessory proteins link double-strand break sites to the chromosome axis in early meiotic recombination. Cell. 2011; 146:372–383. [PubMed: 21816273]
17. Arora C, Kee K, Maleki S, Keeney S. Antiviral protein Ski8 is a direct partner of Spo11 in meiotic DNA break formation, independent of its cytoplasmic role in RNA metabolism. Mol Cell. 2004; 13:549–559. [PubMed: 14992724]
18. Sommermeyer V, Beneut C, Chaplais E, Serrentino ME, Borde V. Spp1, a member of the Set1 Complex, promotes meiotic DSB formation in promoters by tethering histone H3K4 methylation sites to chromosome axes. Mol Cell. 2013; 49:43–54. [PubMed: 23246437]
19. Acquaviva L, et al. The COMPASS subunit Spp1 links histone methylation to initiation of meiotic recombination. Science. 2013; 339:215–218. [PubMed: 23160953]
20. Kumar R, et al. MEI4 - a central player in the regulation of meiotic DNA double-strand break formation in the mouse. J Cell Sci. 2015; 128:1800–1811. [PubMed: 25795304]
21. Stanzione M, et al. Meiotic DNA break formation requires the unsynapsed chromosome axis-binding protein IHO1 (CCDC36) in mice. Nat Cell Biol. 2016; 18:1208–1220. [PubMed: 27723721]
22. Robert T, Vrielynck N, Mezard C, de Massy B, Grelon M. A new light on the meiotic DSB catalytic complex. Semin Cell Dev Biol. 2016; 54:165–176. [PubMed: 26995551]
23. Tesse S, et al. Asy2/Mer2: an evolutionarily conserved mediator of meiotic recombination, pairing, and global chromosome compaction. Genes Dev. 2017; 31:1880–1893. [PubMed: 29021238]
24. Wang W, et al. Homozygous mutations in REC114 cause female infertility characterised by multiple pronuclei formation and early embryonic arrest. Journal of medical genetics. 2019
25. Kumar R, et al. Mouse REC114 is essential for meiotic DNA double-strand break formation and forms a complex with MEI4. Life science alliance. 2018; 1:e201800259. [PubMed: 30569039]
26. Kumar R, Bourbon HM, de Massy B. Functional conservation of Mei4 for meiotic DNA double-strand break formation from yeasts to mice. Genes Dev. 2010; 24:1266–1280. [PubMed: 20551173]
27. Boekhout M, et al. REC114 Partner ANKRD31 Controls Number, Timing, and Location of Meiotic DNA Breaks. Mol Cell. 2019; 74:1053–1068.e1058. [PubMed: 31003867]
28. Engebrecht JA, Voelkel-Meiman K, Roeder GS. Meiosis-specific RNA splicing in yeast. Cell. 1991; 66:1257–1268. [PubMed: 1840507]
29. Lorenz A, Estreicher A, Kohli J, Loidl J. Meiotic recombination proteins localize to linear elements in Schizosaccharomyces pombe. Chromosoma. 2006; 115:330–340. [PubMed: 16532353]
30. Bonfils S, Rozalen AE, Smith GR, Moreno S, Martin-Castellanos C. Functional interactions of Rec24, the fission yeast ortholog of mouse Mei4, with the meiotic recombination-initiation complex. J Cell Sci. 2011; 124:1328–1338. [PubMed: 21429938]

31. Li P, et al. Phase transitions in the assembly of multivalent signalling proteins. Nature. 2012; 483:336–340. [PubMed: 22398450]
32. Wheeler JR, Matheny T, Jain S, Abrisch R, Parker R. Distinct stages in stress granule assembly and disassembly. Elife. 2016; 5
33. Su X, et al. Phase separation of signaling molecules promotes T cell receptor signal transduction. Science. 2016; 352:595–599. [PubMed: 27056844]
34. Boulay G, et al. Cancer-Specific Retargeting of BAF Complexes by a Prion-like Domain. Cell. 2017; 171:163–178.e119. [PubMed: 28844694]
35. Banani SF, Lee HO, Hyman AA, Rosen MK. Biomolecular condensates: organizers of cellular biochemistry. Nat Rev Mol Cell Biol. 2017; 18:285–298. [PubMed: 28225081]
36. Boeynaems S, et al. Protein Phase Separation: A New Phase in Cell Biology. Trends in cell biology. 2018; 28:420–435. [PubMed: 29602697]
37. Lin Y, Protter DS, Rosen MK, Parker R. Formation and Maturation of Phase-Separated Liquid Droplets by RNA-Binding Proteins. Mol Cell. 2015; 60:208–219. [PubMed: 26412307]
38. Patel A, et al. A Liquid-to-Solid Phase Transition of the ALS Protein FUS Accelerated by Disease Mutation. Cell. 2015; 162:1066–1077. [PubMed: 26317470]
39. Xiang S, et al. The LC Domain of hnRNPA2 Adopts Similar Conformations in Hydrogel Polymers, Liquid-like Droplets, and Nuclei. Cell. 2015; 163:829–839. [PubMed: 26544936]
40. Garcia V, Gray S, Allison RM, Cooper TJ, Neale MJ. Tel1(ATM)-mediated interference suppresses clustered meiotic double-strand-break formation. Nature. 2015; 520:114–118. [PubMed: 25539084]
41. Johnson D, et al. Concerted cutting by Spo11 illuminates the mechanism of meiotic DNA break formation. Nature. 2021
42. Dosztanyi Z. Prediction of protein disorder based on IUPred. Protein Sci. 2018; 27:331–340. [PubMed: 29076577]
43. Sebastiaan Winkler G, et al. Isolation and mass spectrometry of transcription factor complexes. Methods. 2002; 26:260–269. [PubMed: 12054882]
44. Erdjument-Bromage H, et al. Examination of micro-tip reversed-phase liquid chromatographic extraction of peptide pools for mass spectrometric analysis. J Chromatogr A. 1998; 826:167–181. [PubMed: 9871337]
45. Yang B, et al. Identification of cross-linked peptides from complex samples. Nat Methods. 2012; 9:904–906. [PubMed: 22772728]
46. Combe CW, Fischer L, Rappsilber J. xiNET: cross-link network maps with residue resolution. Molecular & cellular proteomics : MCP. 2015; 14:1137–1147. [PubMed: 25648531]
47. Nesvizhskii AI, Keller A, Kolker E, Aebersold R. A statistical model for identifying proteins by tandem mass spectrometry. Anal Chem. 2003; 75:4646–4658. [PubMed: 14632076]
48. Murakami H, Borde V, Nicolas A, Keeney S. Gel electrophoresis assays for analyzing DNA double-strand breaks in Saccharomyces cerevisiae at various spatial resolutions. Methods Mol Biol. 2009; 557:117–142. [PubMed: 19799180]
49. Neale MJ, Keeney S. End-labeling and analysis of Spo11-oligonucleotide complexes in Saccharomyces cerevisiae. Methods Mol Biol. 2009; 557:183–195. [PubMed: 19799183]